UNIVERSITY OF OKLAHOMA

GRADUATE COLLEGE

WEAK ANTI-LOCALIZATION STUDIES OF SPIN-ORBIT COUPLIN IN N- AND P-TYPE InSb HETEROSTRUCTURES

A DISSERTATION

SUBMITTED TO THE GRADUATE FACULTY

in partial fulfillment of the requirements for the

Degree of

DOCTOR OF PHILOSOPHY

By

P. A. RENUKA DILHANI JAYATHILAKA
Norman, Oklahoma
2012

WEAK ANTI-LOCALIZATION STUDIES OF SPIN-ORBIT COUPLING IN N- AND P-TYPE InSb HETEROSTRUCTURES

A DISSERTATION APPROVED FOR THE
HOMER L. DODGE DEPARTMENT OF PHYSICS AND ASTRONOMY

BY

_____
Dr. Sheena Q. Murphy, Chair

_____
Dr. Michael Santos

_____
Dr. Kieran Mullen

_____
Dr. Matthew Johnson

_____
Dr. Rui Q. Yang

This thesis is dedicated to my parents!

Acknowledgement

First and foremost, I would like to express my deepest gratitude to my thesis advisor Dr. Sheena Q. Murphy for her guidance, support and expertise whenever and wherever it was needed during my research. Her great supervision helped me throughout the process of writing this thesis.

Besides my advisor, I would like to sincerely thank the rest of my thesis committee: Dr. Michael B. Santos, Dr. Matthew B. Johnson, Dr. Kieran Mullen and Dr. Rui Q. Yang for their guidance, invaluable comments and suggestions in completing this work. I also thank to my former committee member Dr. Roger Frech. I really appreciated his help when I was working his lab.

My special thanks go to Dr. Joel Keay, whose invaluable assistance and guidance in instrument handling made my research successful. In addition, Dr. Joel Keay taught me electron beam lithography, helped me to fabricate the narrow wires in this work. I also thank and appreciate Dr. Preston Larson for his enthusiastic support of my work in the microscopy lab.

Furthermore, I am thankful to my former and present lab colleagues Ruwan Dedigama, Jon Caddell and Shanye Cairns, all of the other members of the solid state group, OU friends and all Sri Lankans friends for their friendship, numerous contributions and assistances to my research work throughout all these years.

All the faculty and staff members of the Department of Physics and Astronomy, the staff of the OU Graduate College and the International Student Services are gratefully acknowledged for helping my work in numerous ways throughout my graduate studies.

I am deeply thankful to my wonderful parents and sisters who have always supported me with their endless love and encouragement during my years in graduate school. Finally, I would like to give my heartfelt appreciation to my husband, Roshan Bokalawela and my two daughters, Nethmi and Rashmi. This thesis work would have been impossible without Roshan's support and encouragement, and without my daughter's beautiful loving smiles.

Table of Contents

List of Tables

List of Figures

Abstract

The effects of spin-orbit interactions (SOIs) on transport properties of InSb/AlInSb heterostructures have been studied experimentally. At low temperatures, the quantum interference gives rise to a quantum correction to the classical Drude conductance. For 2D systems, the dominant quantum corrections are due to weak anti-localization (WAL) and electron-electron interaction effects. This thesis is concerned with these contributions.

The first part of this dissertation describes the development of device fabrication processes for InSb material, including electron beam lithography (EBL) and dry etching (RIE). The second part describes two separate magneto-transport measurements performed in 2D electron and hole systems as well as in 1D wire arrays fabricated from 2D electron gases. Both experiments employ low field magneto-transport measurements to explore the SOI.

Spin-orbit effects in III-V semiconductor heterostructures arise from two distinct inversion asymmetries: bulk inversion asymmetry (Dresselhaus) and structural inversion asymmetry (Rasha), due to crystalline anisotropy in III-V zincblende crystal and heterointerface, respectively. In the first set of experiments, we studied symmetrically doped InSb/AlInSb heterostructures with comparable magnitude spin orbit contributions from both linear and cubic Dresselhaus. In this limit the spin-split Fermi surface are four-fold symmetric and present minimal and maximal spin-orbit (SO) fields along the [100] and [110] direction, respectively.

For this experiment, Hall bars (HB) and arrays of quasi-1D wires were patterned along these crystallographic directions for a (100) growth plane to reveal the anisotropic spin-split Fermi surface. The arrays of 1D wires were fabricated using EBL and reactive ion etching. Using weak localization (WL) analysis, we calculated a Dresselhaus constant $\gamma = 520\pm20$ eVÅ^3 for our particular InSb QW, in very good agreement with the theoretically predicted value. Suppression of spin relaxation was observed as the channel was narrowed and wires aligned along the [100] direction displayed spin relaxation lengths ~30% longer than for wires aligned along [110] due to the additional influence of the cubic Dresselhaus which is predicted to be unaffected by dimensional confinement. Additionally in the diffusive regime, electron–electron scattering responsible for dephasing was investigated as a function of temperature.

The second set of experiments focused on the geometry dependence of Rashba spin splitting of the valence band (VB) in the 2D hole system. In a 2D hole system, the Rashba coupling can be modified by varying the carrier concentration and by changing the confinement. Compared to the 2DE system, we observed a huge spin splitting, ~2-5meV. While the observed spins splitting were in qualitative agreement with theoretical expectation, there was substantial quantitative disagreement.

Dissertation Outline

Over the last two decades, interest has grown in studying spin dynamics and transport due to the potential for spintronics based devices. Spin injection, transport, manipulation and detection are the four main elements required for a spintronic device. In this dissertation, we are concerned with spin transport and relaxation in InSb. Electrons and holes in InSb have strong spin-orbit coupling (SOC) compared to the other III-V materials. Since InSb is relatively uncommon material, its spin transport has not been explored to the extent of other III-V materials. Thus, determination of spin relaxation in InSb based quantum wells (QW) is critical because it provides fundamental information relevant to spin transport. Using transport techniques, it is common to study the spin relaxation mechanisms via measurements of the interference in low field magneto-resistance at low temperature. Ignoring the carrier spin, this quantum interference effect which results in constructive interference (weak localization) was first predicted by Anderson in 1958 for metallic systems [1, 2]. Later a qualitative explanation for quantum interference was given by Bergmann for thin metallic films [3].

In 1980, Hikami et al evaluated the effect of spin on the WL, which resulted in a change from destructive to constructive interference (weak anti-localization) [4]. Later more complex modifications were incorporated [3-8] and have since been applied to various III-V systems via transport experiments [9-19]. The first demonstration of the suppression of spin relaxation due to geometrical confinement was performed by Th.Schapers *et al*. using WAL analysis of InGaAs

(2006) [20]. At the same time, Holleitner et al. demonstrated the anisotropic spin relaxation in 1D InGaAs wires via an optical experiment [21]. However, anisotropic spin relaxation in 1D wires has not been demonstrated via transport, hence, the justification for these experiments to study anisotropic spin relaxation in 1D InSb channels along [100] and [110] directions by WAL.

Additionally, little work has been performed on hole systems. Theoretical work has shown that Rashba coefficients can be modified by changing the QW width [22]. In the second part of the thesis, we investigated the WAL in p-type InSb/AlInSb QWs, studying the impact of well width on WAL. These are the first WAL studies in p-type InSb.

This dissertation is divided into six chapters organized in the following way: Chapter I consists of fundamental background on the SOI in solid systems, in which a theoretical overview of the Rashba and Dresselauus SOI is described.

Chapter II contains the basic concepts and theoretical overview necessary to understand the quantum interference of the low dimensional system studied in this work. In subsequent sections, I will discuss the conductance, the quantum interference effects, the relevant theoretical models and the suppression of spin relaxation in the 1D electron system.

The third chapter reviews the fabrication techniques employed in this work. This includes a detailed account of the optical and EBL and dry and wet etching

techniques that were used to fabricate InSb/AlInSb devices. In chapter IV, the details of InSb QW structures are given.

Chapters V and VI are experimental chapters. In chapter V, I will present the results of magneto-transport in two dimensional electron systems (2DESs). The first part of the chapter focuses on understanding the SOI and electron transport through InSb 2DESs at low-temperature. The second part of the chapter focuses on changes of the spin relaxation length and anisotropy in spin relaxation related to narrowed conducting channel fabricated from the 2DES. These measurements are analyzed in terms of the theoretical predictions presented in chapter II in the temperature range 1.5K to 10K. In the last part of the chapter, the results of electron-electron interaction in both 2D and 1D limits are discussed.

The experiment described in chapter VI focuses on investigating the Rashba SOI of the 2D hole gas in Be-doped InAlAs/InSb QWs, as a function of carrier concentration and well width. These measurements are analyzed in terms of the theoretical predictions for the 2D hole gas system presented in chapter II. Furthermore, experimental results are compared with the theory developed by the means of the Extended Kane Model for the heavy hole (HH) in the VB. Chapter VII provides conclusions and suggestions for future work. The dissertation concludes with a list of references.

Chapter 1: Fundamentals of the Spin-Orbit Interaction in Solid Systems

1.1 Introduction

This chapter presents a brief introduction to the origins of the SOI in a solid state system. In a solid system, the correlation between the orbital motion and the particle spin is an important relativistic effect which can lift the spin degeneracy even in zero applied magnetic field. The SOI coupling can be derived from the non-relativistic limit of the Dirac-equation [23] and is expressed as:

$$\mathrm{H_{so}} = \frac{e\hbar^2}{4\mathrm{m_o^2 c^2}}\boldsymbol{\sigma}\left(\mathbf{k}\times\nabla\mathrm{V}\right) \qquad 1.1$$

Here, $\mathrm{m_o}$ is the free electron mass, c is the speed of the light, $\boldsymbol{\sigma}$ is the Pauli spin matrices, $\mathbf{k} = 2\pi\mathbf{p}/\mathrm{h}$ is the wave vector and V is the potential, where the gradient of the potential is minus the electric field (E).

The SOI has different physical origins as will be discussed in the subsections below. In the laboratory frame a particle can move in a region with a non-zero electric field; in the rest frame of the particle, however, the particle feels an effective magnetic field due to the Lorentz transformation of the electric field (see Figure 1.1). The magnitude of this effective magnetic field is given by the standard Lorentz transformation [24],

$$\mathbf{B}_{\mathrm{eff}} = \frac{-\gamma\left(\mathbf{v}\times\mathbf{E}\right)}{\mathrm{c}^2} = \frac{-\gamma\left(\mathbf{p}\times\mathbf{E}\right)}{\mathrm{mc}^2} \qquad 1.2(a)$$

where, $\gamma = 1/\sqrt{1-(v/c)^2}$ is the Lorentz factor and v is the velocity of the particle. For a slow particle, $(v/c)^2 << 1$, one can neglect the higher order terms in $(v/c)^2$. Then the effective magnetic field reduces to,

$$\mathbf{B}_{\text{eff}} = \frac{-(\mathbf{p}\times\mathbf{E})}{mc^2}. \qquad 1.2(b)$$

It is this momentum dependent effective magnetic field that causes the coupling between the spin and the orbital motion.

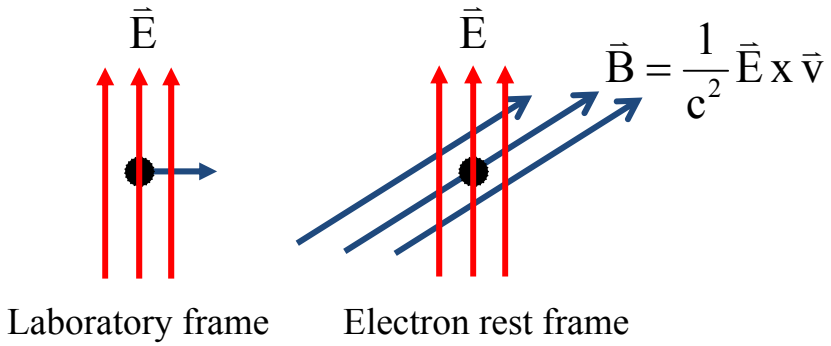

Figure 1.1 The motion of the electron in a region with a non-zero electric field: (a) lab frame (b) rest frame [25].

1.2 Spin-Orbit Interaction in a Two-Dimensional System

In general the effect of the SOI is to lift the spin degeneracy of the carrier (electron or hole) states in a semiconductor. The spin degeneracy arises from the combined effects of inversion symmetry in space and time [22].

$$\left.\begin{array}{l}\text{Spatial inversion symmetry}, E(\mathbf{k},\uparrow) = E(-\mathbf{k},\uparrow)\\ \text{Time inversion symmetry}, E(\mathbf{k},\uparrow) = E(-\mathbf{k},\downarrow)\end{array}\right\} \quad E(\mathbf{k},\uparrow) = E(\mathbf{k},\downarrow) \qquad 1.3$$

If the spatial inversion symmetry is broken, $E(\mathbf{k},\uparrow) \neq E(-\mathbf{k},\uparrow)$, then there are two branches for the single particle energy dispersion even in the absence of an external magnetic field (see Figure 1.2), (i.e. spin splitting).

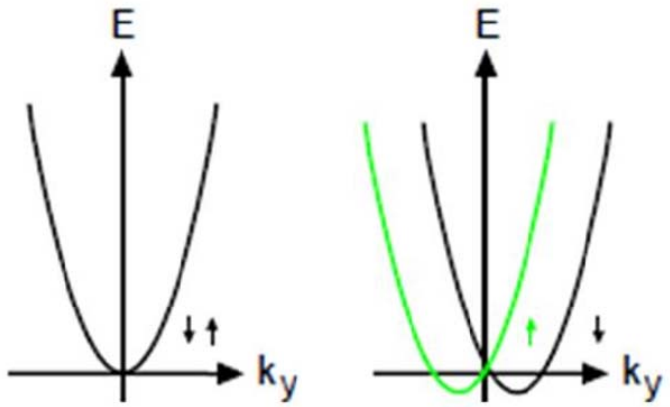

Figure 1.2 Energy dispersion relations for spin spilt bands [25].

In quasi-two dimensional (2D) semiconductor structures without a center of inversion symmetry, it is well known that two distinct electric fields are involved in spin splitting; they are however different in physical nature. The first is a crystal field associated with bulk inversion asymmetry (BIA) of the bulk host material also known as the Dresselhaus SOI [25, 27]. The second is caused by the structural inversion asymmetry (SIA) of the heterostructure itself also known as the Rashba SOI. This SOI was first introduced by Rashba in the 1960's for semiconductor materials [28] and was later developed with more details by

Bychkov and Rashba to describe and analyze experimental data in the term of SOI for the 2DEG [29,30].

As mentioned earlier, in the rest frame of the carrier, these fields are transformed into **k** dependent effective magnetic fields, which result in an energy difference between the spin-up (↑) and the spin-down (↓) bands in both the conduction and valence bands. The spin of the carrier precesses around this superposition of effective magnetic fields. The corresponding Hamiltonian for conduction electrons in a III-V semiconductor structure grown along the [001] direction can be then written as [7, 8, 31-35]:

$$\mathrm{H} = \frac{\hbar^2 \mathbf{k}^2}{2\mathrm{m}^*} + (\boldsymbol{\sigma}.\boldsymbol{\Omega}(\mathbf{k})) \qquad 1.4$$

Here, the first term is kinetic energy and the second term is the SO energy which describes the lifting of the two fold spin degeneracy at $\mathbf{k} \neq 0$. In a 2D system, $\boldsymbol{\Omega}$ is an odd function of the in-plane wave vector, **k**. This spin precession frequency is related to the spin splitting energy ($\Delta \mathrm{E}$) and is given by [8, 36, 37]:

$$\left|\boldsymbol{\Omega}(\mathbf{k})\right| = \frac{\Delta \mathrm{E}}{2\hbar} \qquad 1.5$$

If both Rashba and Dresselhaus SOIs are present in the 2D system, the vector $\boldsymbol{\Omega}(\mathbf{k})$ is the combination and can be written as [7, 8]:

$$\boldsymbol{\Omega}(\mathbf{k}) = \boldsymbol{\Omega}_{\mathrm{R}}(\mathbf{k}) + \boldsymbol{\Omega}_{\mathrm{D}}(\mathbf{k}) \qquad 1.6$$

Where, the vectors $\mathbf{\Omega_R(k)}$ and $\mathbf{\Omega_D(k)}$ are the Rashba and the Dresselhaus spin precession frequencies respectively.

1.2.1 Dresselhaus Spin-Orbit Interaction in the 2D Electron Gas

In a bulk crystal, the spin splitting is accounted for by a pure Dresselhaus SOI. Ordinary A_3B_5 bulk crystals such as InSb and GaAs have a zinc-blende structure [8] and the spin splitting of the conduction band (CB) is then described by the following Hamiltonian [8, 26]:

$$\begin{aligned} H_D &= \sigma.\Omega_D(k) \\ &= \gamma\left[\sigma_x k_x (k_y^2 - k_z^2) + \sigma_y k_y (k_z^2 - k_x^2) + \sigma_z k_z (k_x^2 - k_y^2)\right] \end{aligned} \qquad 1.7$$

Where, γ is the Dresselhaus coefficient which depends on the material and cannot be tuned. Compared to the other III-V semiconductors, the theoretically predicted value of γ for InSb is very large (ranging from $560 < \gamma < 760$ eVÅ^3 [22, 33, 38]. For InAs and GaAs materials γ is about ~27 eVÅ^3. According to Equation 1.7, the Dresselhaus spin splitting is proportional to the cube of the electron wave vector $\mathbf{k} = (k_x, k_y, k_z)$. When the Dresselhaus SOI is applied to a 2D system grown along the [001] direction, the expectation value of $\langle k_z \rangle$ is zero, while $\langle k_z^2 \rangle$ is quantized as a result of quantum confinement; thus, in addition to terms cubic in the momentum, the Hamiltonian of the 2D system also has k-linear Dresselhaus

terms [8, 22, 31, 39, 40] as can be seen after substituting, $\langle k_z \rangle = 0$ and $\langle k_z^2 \rangle \neq 0$ into equation 1.7, yielding the following form:

$$H_D = \sigma.\Omega_D(k) = \sigma_x.\Omega_{x,D}(k) + \sigma_y.\Omega_{y,D}(k)$$
$$= \gamma\left[-\langle k_z^2 \rangle(\sigma_x k_x - \sigma_y k_y) + (k_y^2 \sigma_x k_x - k_x^2 \sigma_y k_y)\right] \quad 1.8$$

Here $\boldsymbol{\Omega}_D(\mathbf{k})$ is the total Dresselhaus spin precession frequency vector of the conduction electron in a zinc-blende QW grown along the [001] crystallographic direction. $\langle k_z^2 \rangle = \int dz \psi^* \left(-\frac{d^2}{dz^2}\right)\psi$ is the mean square of the electron momentum in the direction of the quantum confinement.

The linear term, $(\sigma_x k_x - \sigma_y k_y)$ is isotropic in the plane of the QW (see Figure 1.3 (a)). The cubic term, $(\sigma_x k_y^2 k_x - \sigma_y k_x^2 k_y)$ is anisotropic in the plane of the QW (see Figure 1.3(b)), with maximum amplitude along the [110] and [1-10] directions. In the case of a narrow QW, the confinement is large, $\langle k_z^2 \rangle >> k_F^2$ and the linear term dominates the spin splitting, and the cubic Dresselhaus contribution is usually neglected in the SO analysis. However, in the case of a wide QW with heavy doping, the relation $\langle k_z^2 \rangle \approx k_F^2$ holds and then both linear and cubic terms contribute to the spin splitting of the CB.

In chapter 5, the InSb CB spin splitting is interpreted in the framework of the Dresselhaus SOI taking into account both linear and cubic contributions.

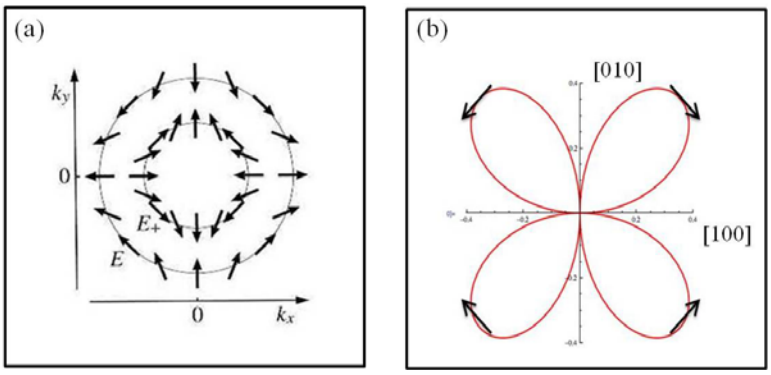

Figure 1.3 The spin orientation of the (a): linear $(\sigma_x k_x - \sigma_y k_y)$ and (b): cubic $(\sigma_x k_y^2 k_x - \sigma_y k_x^2 k_y)$, Dresselhaus terms as a function of the in-plane wave vector for the zinc-blende type QWs. Arrows indicate the directions of the spin orientation.

1.2.2 Rashba Spin-Orbit Interaction in the 2D Hole Gas

The Rashba SOI is important only in 2D systems where the confining potential is asymmetric. When considering electrons, an asymmetry in the potential and band offsets of the barrier materials leads to a non-zero electric field in the VB across the heterostructures perpendicular to the plane of electron motion [22]. Figure 1.4 shows the confining potential of the CB for an asymmetric QW. A moving electron feels the electric field as an effective magnetic field in the plane of the QW perpendicular to the electron motion and electric field.

In order to get a simpler picture of the Rashba field which controls the spin splitting, we assumed the 2DE system was confined along z-axis. If only the

lowest conduction subband is occupied, the Hamiltonian describing the QW can be written as:

$$H_c = \frac{\hbar^2 \mathbf{k}_z^2}{2m^*} + U(z) = \frac{\mathbf{p}_z^2}{2m^*} + U(z) \qquad 1.9$$

where, the potential energy $U(z) = qV_c(z)$ in which $V_c(z)$ is the electric potential and q is the charge. Here, we have assumed a position-independent effective mass. The expectation value of the time evolution of the momentum operator in a bound state of H_c is given by,

$$\left\langle \frac{dp_z}{dt} \right\rangle_c = \frac{1}{i\hbar} \langle \varphi_c | [p_z, H_c] | \varphi_c \rangle \qquad 1.10$$

(Ehrenfest theorem)

$$\left\langle \frac{dp_z}{dt} \right\rangle_c = \langle qE_c(z) \rangle_c = \langle F_E(z) \rangle_c = 0 \qquad 1.11$$

Where $\langle \varphi_c |$ describes a bound state and the force on an electron in the CB $\langle F_E(z) \rangle_c = 0$. So that $\langle qE_c(z) \rangle = 0$. Hence, the potential dependent band energies result in a non-zero $E_v(z)$ valence band **E** where contributes to the Rashba spin splitting.

In a 2D electron system, the Rashba spin splitting has a linear k dependence and is proportional to the degree of asymmetry of the heteropotential. More details of the Rashba spin splitting for the electron system are described in Ref. [22].

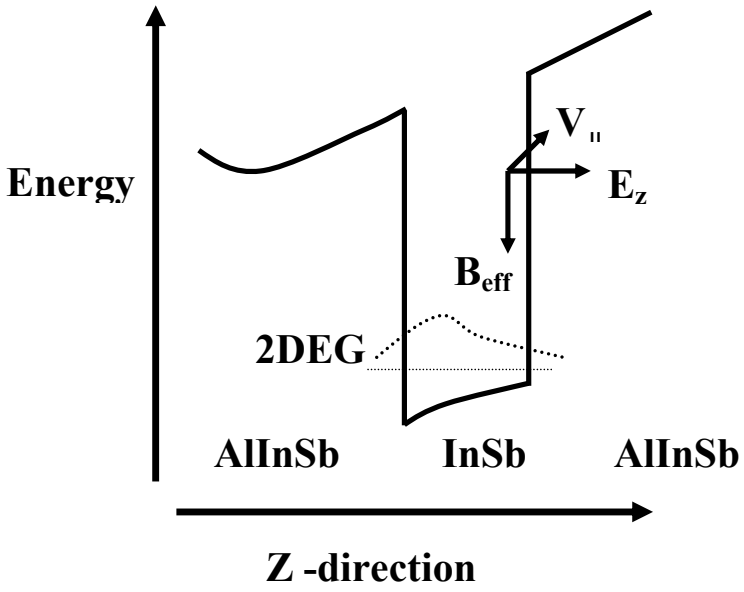

Figure 1.4 Schematic conduction band diagrams for an asymmetric QW. If the electric field (E_z) is along the growth direction, an effective magnetic field ($B_{eff}(k)$) is induced in the plane of the QW, perpendicular to the momentum of the electron.

Unlike the 2D electronic system, the Rashba spin splitting of the two-dimensional hole system (2DHS) is more complicated due to the mixing of the heavy hole (HH) and light hole (LH) bands. However, the confinement is usually large enough to separate the HH (M_J =3/2) and LH (M_J=1/2) bands, so that they can be treated independently. To lowest order, the Rashba spin splitting of LH and HH are first and third order in the wave vector respectively. If the QW is confined in

the direction of z-axis such that only the lowest HH band is occupied, the resulting Rashba Hamiltonian for the HH in the Γ_8^v VB is given by [22]:

$$H_{HH}^{R} = \beta k * E_z \cdot J \qquad 1.12$$

In this equation, **J** is the angular momentum matrices for j=3/2 along the x, y and z directions and β is the Rashba coefficient which depends on the structure itself. Starting from the 8x8 extended Kane Model, the above Hamiltonian has been expanded in Ref [22] as:

$$H_{HH}^{R} = \sigma.\Omega_{HH}^{R}(k) = \sigma.\left(\Omega_{53,HH}^{R}(k) + \Omega_{54,HH}^{R}(k)\right)$$

$$H_{HH}^{R} = \gamma_{53}^{7H,7H} i\left(\left\{k_+, k_-^2\right\}\sigma_- - \left\{k_+^2, k_-\right\}\sigma_+\right)E_z + \gamma_{54}^{7H,7H} i\left(k_+^3, \sigma_- - k_-^3, \sigma_+\right)E_z \qquad 1.13$$

Notation: $\{A, B\} = \frac{1}{2}(AB + BA)$

In this equation, $\sigma_\pm = 1/2\,(\sigma_x \pm i\sigma_y)$ and $k_\pm = k_x \pm ik_y$ and $\gamma_{53}^{7H,7H}$ and $\gamma_{54}^{7H,7H}$ are the Rashba coefficients to be discussed below. By substituting plane polar, coordinates, $k_y = k_F \cos\theta$, $k_y = k_F \sin\theta$ and the Fermi wave vector, $k_F = \sqrt{k_x^2 + k_y^2}$), equation 1.13 can be rewritten as:

$$\Omega_{HH}^{R} = \begin{pmatrix} \left[\sigma_x k_F^3 \left(E_z \gamma_{53}^{7H,7H}\right)\sin\theta + \sigma_y k_F^3 \left(E_z \gamma_{53}^{7H,7H}\right)\cos\theta\right] + \\ \left[\sigma_x k_F^3 \left(E_z \gamma_{54}^{7H,7H}\right)\sin 3\theta + \sigma_y k_F^3 \left(E_z \gamma_{54}^{7H,7H}\right)\cos 3\theta\right] \end{pmatrix} \quad 1.14$$

Here, we can see from this expression that spin precession frequencies related to $\gamma_{53}^{7H,7H}$ and $\gamma_{54}^{7H,7H}$ can be separated according to angle θ and 3θ yielding the following form:

$$\Omega_{53,HH}^{R}(k) = k_F^3 E_z \gamma_{53}^{7H,7H}(\sin\theta, \cos\theta)$$
$$\Omega_{54,HH}^{R}(k) = k_F^3 E_z \gamma_{54}^{7H,7H}(-\sin 3\theta, \cos 3\theta) \quad 1.15$$

Treating the off-diagonal HH-LH coupling by using third order perturbation theory, both $\gamma_{53}^{7H,7H}$ and $\gamma_{54}^{7H,7H}$ are given by Ref. [22, 41] as:

$$\gamma_{53}^{7H,7H} = \frac{3}{4}\frac{e\hbar^4}{m_o^2}\gamma_3(\gamma_2 - \gamma_3)\left(\frac{1}{\Delta_{HL}^2} - \frac{1}{\Delta_{HS}^2}\right) \quad 1.16(a)$$

$$\gamma_{54}^{7H,7H} = \frac{3}{4}\frac{e\hbar^4}{m_o^2}\gamma_3(\gamma_2 + \gamma_3)\left(\frac{1}{\Delta_{HL}^2} - \frac{1}{\Delta_{HS}^2}\right) \quad 1.16(b)$$

In these equations, Δ_{HL} and Δ_{HS} are the energy gaps between HH and LH bands and HH and split-off bands (Δ_0) respectively and γ_2 and γ_3 are the Luttinger parameters for the InSb material [22] are:

$$\gamma_3 = 17.70$$
$$\gamma_2 = 16.50$$
$$\Delta_0 = 0.8\text{eV}$$

As seen in equations 1.16 (a) and (b), both $\gamma_{53}^{7H,7H}$ and $\gamma_{54}^{7H,7H}$ are not fixed and can be modified by changing the QW width, i.e. changing the HH and LH band separation. When the QW is narrowed, the Δ_{HL} value increases, resulting in a smaller Rashba parameter. Comparison the two expression in 1.16, the leading Rashba coefficient is $\gamma_{54}^{7H,7H}$ as the prefactor $\gamma_3(\gamma_2+\gamma_3)$, for InSb $\gamma_{54}^{7H,7H}$ is 28x larger than $\gamma_{53}^{7H,7H}$. The product of $\gamma_{54}^{7H,7H}$ and E_z is the Rashba coupling constant. In general, E_z increases when the density of the system is increased and since the well potential can also be modified by application of an external electric field, the Rashba coupling can be varied by means of an external gate as has been experimentally demonstrated by G. M. Minkov *et al.* in a InGaAs 2DHG system [42]. According to equation 1.13, the Rashba spin split HH sub band dispersion is given as [22]:

$$E_{HH}^{R}(k_F) = \frac{\hbar^2 k_F^2}{2m_{HH,x,y}^{*}} \pm \gamma_{54}^{7H,7H} E_z k_F^3 \qquad 1.17$$

Here, the first term is the kinetic energy corresponding to the HH where $m_{HH,x,y}$ is the in-plane HH effective mass and the second term is the HH Rashba spin splitting energy. In chapter 6, the Rashba spin splitting of the 2D InSb hole system was evaluated by taking into account expressions 1.16(b).

1.3 D'yakonov-Perel Mechanism and Spin Relaxation

The D'yakonov-Perel mechanism (DP) dominates, for systems which lack inversion symmetry (zincblende crystal structure) resulting in lifting the spin degeneracy of the CB and VB in all directions [26]. This spin splitting of the CB/VB is analogous to an internal k-dependent effective magnetic field, B(k), acting on the electron spin as described in section 1.1. The spin of the electron/hole precesses about this effective magnetic field with Larmor frequency, $\Omega(k)=(e/m)B(k)$. When an electron is scattered from one momentum state, k, to another momentum state, k', the direction and the magnitude of the effective magnetic field is randomized with scattering, changing with every carrier scattering event, ($B(\mathbf{k})\rightarrow B(\mathbf{k}')$) (Figure 1.5). The precession frequency also changes ($\Omega(\mathbf{k})\rightarrow\Omega(\mathbf{k}')$). After a number of scattering events, the spin of the electron/hole completely loses its spin memory undergoing spin relaxation.

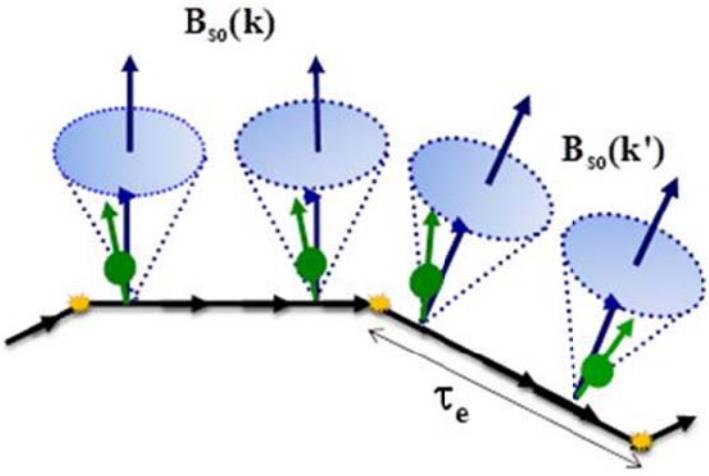

Figure 1.5 Schematic view of the D'yakonov-Perel mechanism. Spin precesses in a different direction after momentum scattering. τ_e is the momentum scattering.

In the case of strong disorder, $\delta\varphi=\Omega(k)\tau_e<<1$, then the spin phase follows a random walk. After certain a time, t:

$$\text{Total phase increment} = \delta\varphi\sqrt{\frac{t}{\tau_e}} \qquad 1.18$$

When, the total phase increment ~1, the time t goes to spin relaxation time, τ_{so}, and equation 1.18 implies,

$$\frac{1}{\tau_{so}} \approx \Omega(k)^2 \tau_e \qquad 1.19$$

i.e. the spin relaxation time is inversely proportional to the momentum scattering time. Then the distance related to the spin relaxation time for spin polarization go to zero is the spin relaxation length, $L_{so} \approx \sqrt{D\tau_{so}}$ where D is diffusion constant ($\frac{v_F^2\tau_e}{2}$ in 2D).

Chapter 2: Quantum Interference in Low Dimensional Systems

2.1 Introduction

Magneto-transport at low magnetic fields is a powerful tool for measuring the strength of the SOC in low-dimensional (1D) systems. There are several ways to do this. The most common are studies of the characteristic beat patterns in Shubnikov–de Haas oscillations (SdH) [43, 44] and the quantum interference correction to the conductance [9-19]. This chapter starts with a brief discussion of the magneto-conductivity, followed by a brief description of the quantum correction to the conductivity for low dimensional systems. The chapter will end with a short review of the suppression of the spin relaxation in 1D system.

2.2 Conductance

Electrical conductivity is the one of the characteristic properties of a conductor. In classical theory, the Drude expression describes the conductivity of an ordinary conductor [45]. In the presence of external electric field (**E**)**,** the carriers (electron or hole) move in the direction of the force $q\mathbf{E}$, where q is the charge of the carrier. The system has impurities, defects and grain boundaries making it disordered, so that, the carrier undergoes scattering events, both elastic (eg. electron-impurity) and inelastic (eg. electron -phonon). At steady state, the rate at which carriers gain momentum from the external electric field must be equal to the rate of the momentum loss due to scattering.

$$\left[\frac{d\mathbf{p}}{dt}\right]_{scattering} = \left[\frac{d\mathbf{p}}{dt}\right]_{field} \quad 2.1$$

$$\frac{mv_d}{\tau} = qE \quad 2.2$$

Here, m is the mass of the carrier, time τ_e is the average scattering time between collisions and $\mathbf{v}_d$ is the drift velocity.

By rearranging Eq. (2.2), the average $\mathbf{v_d}$ of the carrier can be written as:

$$\mathbf{v}_d = \left(\frac{q\tau}{m^*}\right)\mathbf{E} \quad 2.3$$

Where the proportionality factor is called the carrier mobility (μ),

$$\mu = \frac{q\tau}{m^*} \quad 2.4$$

which depends on the scattering time. The current density (**J**) is related to the carrier density (n) and $\mathbf{v_d}$ by,

$$\mathbf{J} = nq\mathbf{v_d} \quad 2.5$$

Using equation 2.3 gives,

$$\mathbf{J} = \left(\frac{nq^2\tau_m}{m^*}\right)\mathbf{E} \quad 2.6$$

Here, the proportionality factor between the **J** and the **E** is called the Drude conductivity (σ_D), which is inverse of the Drude resistivity (ρ_D),

$$\sigma_D = \frac{1}{\rho_D} = \frac{nq^2\tau}{m^*} \qquad 2.7$$

If n is constant, σ_D is only changed with τ_e. As one lowers the temperature, σ_D rises due to the suppression of phonon scattering. The Drude model assumes that the electrons do not interfere with each other. When the temperature falls further, σ_D approaches a constant value; the residual resistivity is then entirely determined by the average impurity concentration in the sample. However in the quantum limit, even after the system reaches low temperature, the resistivity of 2D or 1D weakly disordered system can change. This effect is more significant in narrow channels than wide ones [46]. The change of the residual resistance at low temperatures is described by a quantum interference effect, described in greater detail below.

In the simultaneous presence of an electric and a weak magnetic field (B), the equation of motion in steady state can be written as:

$$\frac{mv_d}{\tau} = q\left[\mathbf{E} + \mathbf{v}_d \times \mathbf{B}\right] \qquad 2.8$$

If we assume that the magnetic field is in z-direction, equation (2.8) in matrix form is,

$$\begin{pmatrix} E_x \\ E_y \end{pmatrix} = \begin{bmatrix} m/q\tau & -B \\ B & m/q\tau \end{bmatrix} \begin{pmatrix} v_x \\ v_y \end{pmatrix} \tag{2.9}$$

where v_x and v_y are the x and y component of the drift velocity and E_x and E_y are the x and y components of the electric field. Substituting $\mathbf{J} = nq\mathbf{v}_d$ and $\mu = q\tau / m$, the tensor equation 2.9 can be re-written as follows,

$$\begin{pmatrix} E_x \\ E_y \end{pmatrix} = \frac{1}{\sigma_D(B=0)} \begin{bmatrix} 1 & -\mu B \\ \mu B & 1 \end{bmatrix} \begin{pmatrix} J_x \\ J_y \end{pmatrix} \tag{2.10}$$

with the resistivity tensor given by,

$$\rho = \frac{1}{\sigma_D(B=0)} \begin{bmatrix} 1 & -\mu B \\ \mu B & 1 \end{bmatrix} \tag{2.11}$$

Here, off-diagonal and diagonal terms are the Hall resistivity (ρ_{xy}, ρ_{yx}) and longitudinal resistivity (ρ_{xx}, ρ_{yy}), respectively.

$$\begin{aligned} -\rho_{xy} &= \rho_{yx} = \frac{B}{qn} \\ \rho_{xx} &= \rho_{xx} = \frac{1}{\sigma_D(B=0)} \end{aligned} \tag{2.12}$$

The Hall resistivity increases linearly with magnetic field, thus, n can be determined by measuring the Hall resistivity as a function of the field. The absolute value of the corresponding proportionality factor is the Hall constant, R_H=1/qn and the sign of the Hall constant determines the carrier type, i.e.,

electron or hole. The longitudinal resistivity however does not depend on the magnetic field.

By inverting equation (2.10), one can re-write the tensor equation as:

$$\begin{pmatrix} J_x \\ J_y \end{pmatrix} = \frac{\sigma_D(B=0)}{1+\mu^2 B^2} \begin{bmatrix} 1 & \mu B \\ -\mu B & 1 \end{bmatrix} \begin{pmatrix} E_x \\ E_y \end{pmatrix} \qquad 2.13$$

Then, the conductivity tensor is given by,

$$\frac{\sigma_D(B=0)}{1+\mu^2 B^2} \begin{bmatrix} 1 & \mu B \\ -\mu B & 1 \end{bmatrix} \qquad 2.14$$

Here, off-diagonal and diagonal terms are the transverse (Hall) and longitudinal classical Drude magneto-conductivities, respectively.

$$\sigma_{xy} = -\sigma_{yx} = \frac{-\sigma_D(B=0)\mu)}{1+\mu^2 B^2} = \frac{\rho_{xy}}{\rho_{xy}^2+\rho_{xx}^2}$$

$$\sigma_{xx} = \sigma_{yy} = \frac{\sigma_D(B=0)}{1+\mu^2 B^2} = \frac{\rho_{xx}}{\rho_{xx}^2+\rho_{xy}^2} \qquad 2.15$$

In general, the total electrical conductivity of a low dimensional weakly disordered system at low temperatures is this classical Drude conductivity plus the quantum corrections to the conductivity. For the devices studied in chapter 5 and chapter 6, the key quantum corrections are due to WAL and electron-electron (hole-hole) interaction effects. Thus, the total electrical conductivity of the low dimensional system (σ_{xx}) can be expressed as:

$$\sigma_{xx} = \sigma_{xx}^{D} + \Delta\sigma_{xx}^{QI} \qquad 2.16$$

In this equation, $\Delta\sigma^{QI}$ refers to the conductivity correction corresponding to the quantum interference.

2.3 Quantum Interference Effect

2.3.1 Quantum Interference Trajectories in Disordered Low Dimensional Systems

The quantum effect is associated with the interference of the carrier wave functions as they diffuse through a disordered system at low temperatures. Quantum mechanically, the carrier is wavelike and can be describe by a wave function.

$$\psi(\mathbf{r}) = \left|\psi_o\right| e^{i\varphi}\chi \qquad 2.17(a)$$

where χ is the spin contribution to the wave function and φ is the phase, which is given by:

$$\varphi = (k.r - Et/\hbar) \qquad 2.17(b)$$

where, **k** is the wave vector and E and t are the energy and time, respectively.

Interference trajectories in a disordered low dimensional system at low temperatures can be divided into two groups [47]. One group consists of non-time reversed trajectories. In non-time-reversed trajectories, the carrier trajectories start at the same starting point, r=0, but end at different and randomized points as

shown in Figure 2.1(a). The interference of the wave functions thus occurs somewhere at a distance r≠0 away from the starting point (as long as they are in phase) leading to universal conductance fluctuations (UCF), which were first described by Lee and Stone in 1985 for metallic systems [48].

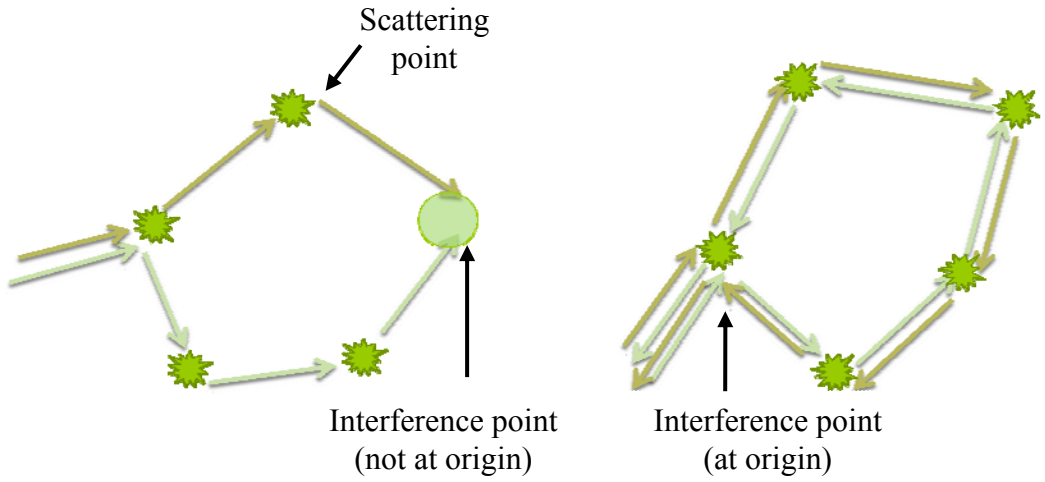

Figure 2.1 Schematic diagrams for the electron trajectories in a disordered system at low temperatures. (a) UCF: Interference of non-time reversed trajectories: A_i and A_j are the probability amplitudes for two trajectories. (b) WL/WAL: Interference of time-reversed trajectories: A_{cw} and A_{ccw} are the probability amplitudes for clockwise and counterclockwise trajectories.

The second set of interference trajectories is time-reversed. For time-reversed trajectories, the trajectories are the same, but are traveled in opposite directions (clockwise and counterclockwise) as seen in Figure 2.1(b). Since these trajectories start and end at the same point, they interfere with each other at the origin, leading to a change in the total probability density, P(r=0,t) for the carrier to return to the origin, as compared to the classical case. There are two possible types of

interference, constructive or destructive. Thus these two types determine which localization effect, either WL or WAL occurs.

2.3.2 Weak Localization

WL was predicted by Anderson in 1958 for metallic systems, ignoring the carrier spin. In 1983, a qualitative explanation for quantum interference was given by Bergmann for thin metallic films [49]. When the carrier spin is ignored, the clockwise and counterclockwise carriers return to the starting point in phase; thus the phase-coherent waves constructively interfere (WL). This effect can be simply understood, if one considers the clockwise path probability amplitude by A_{cw} and counter-clockwise one by A_{ccw}. Then, the total probability of the carriers returning to the starting point after time t, P(r=0, t), is [49]:

$$P(r=0,t) = \sum_i |A_i|^2$$

$$= \left[A_{cw}^2 + A_{ccw}^2\right] \qquad \text{Classical case} \qquad 2.18$$

$$P(r=0,t) = \left|\sum_i A_i\right|^2 = \sum_i |A_i|^2 + \sum_{i \neq j} \mathrm{Re}\, A_i A_j^*$$

$$= \left[A_{cw}^2 + A_{ccw}^2\right] + \left[A_{cw} A_{ccw}^* + A_{ccw} A_{cw}^*\right] \quad \text{Quantum case} \qquad 2.19$$

where, A_i^* is the complex conjugate of A_i. In the classical case, the phase factor has no effect on the transport; thus, P(r=0, t) is the sum of the squares of the probability amplitudes of both trajectories separately. In the quantum case, the

first term is the classical contribution to the total probability and the second cross term reflects the interference, relevant only as long as the carriers are phase coherent. The interference causes an increase in the probability of the finding the carriers at the starting point relative to the classical case. Since the clockwise and counter-clockwise trajectories are the same, $A_{cw}=A_{ccw}=A$ and thus in the quantum case, the probability of return is twice that obtained classically resulting in a suppressed conductance (see Figure 2.2(a)).

$$P(r=0,t)=\left|\sum_i A_i\right|^2=|A_1|^2+|A_2|^2+2|A_1A_2|=4A^2 \qquad 2.20$$

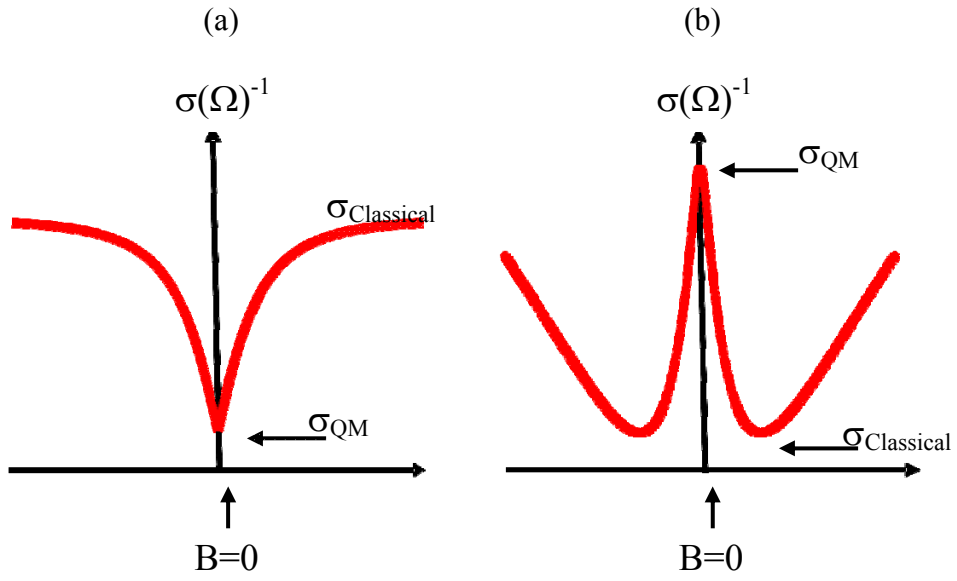

Figure 2.2 Time reversed trajectories: (a) Decreased conductivity at B=0 (WL).(b) Increased conductivity at B=0 (WAL).

Experimentally, this is observed as an increase (decrease) in the resistance (conductance) over the Drude resistance (conductance).

2.3.3 The Effect of Spin on Weak Localization Corrections

In the preceding discussion, we have ignored the carrier spin, but it is interesting to note the influence of the SOC on the phase. In 1980, Hikami *et al*. pointed out that SOC rotates the spin of the carrier which leads to destructive interference between time reversed trajectories [4]. Later, this was demonstrated by Bergmann et al. using the spin rotation matrix, R defined by an Euler angles. The matrix, R written in Ref. 50 has following form (see Figure 1 in Ref. 50),

$$R = \begin{pmatrix} \cos\frac{\theta}{2}\exp[i(\varphi+\beta)] & i\sin\frac{\theta}{2}\exp[-i(\varphi-\beta)] \\ i\sin\frac{\theta}{2}\exp[i(\varphi-\beta)] & \cos\frac{\theta}{2}\exp[-i(\varphi+\beta)] \end{pmatrix} \qquad 2.21$$

The angles, θ and φ describe rotation about the z axis and the angle, β is the rotation of the x-y plane around the z axis [see Feynman lecture III, page 6-12]. Bergmann's explanation can be simply understood, if one considers an initial spin state by $|s\rangle$ and final spin states $|s'\rangle$ and $|s''\rangle$ of two time reversed trajectories.

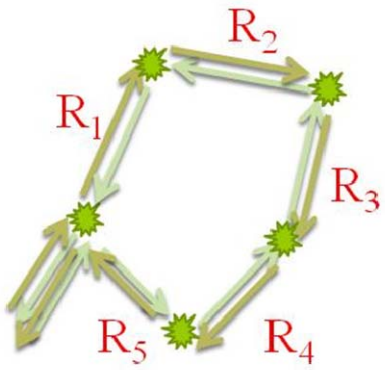

Figure 2.3 Interference of time-reversed trajectories. R_i is the spin rotation between two collisions. $R=R_1R_2\ldots.R_5$.

Since the spin is rotated during each scattering process, $|s'\rangle$ and $|s''\rangle$ can be expressed in terms of the spin rotation operator.

For the clockwise trajectory,

$$\left|s'\right\rangle = R_N R_{N-1} \ldots\ldots\ldots R_3 R_2 R_1 \left|s\right\rangle = R\left|s\right\rangle \qquad 2.22$$

The counter clockwise trajectory experiences the same rotations but in the opposite order,

$$\left|s''\right\rangle = R_1^{-1} R_2^{-1} R_3^{-1} \ldots\ldots\ldots R_{N-1}^{-1} R_N^{-1} \left|s\right\rangle = R^{-1}\left|s\right\rangle \qquad 2.23$$

Due to the property of R,

$$R^{+}R = 1 \qquad R^{-1} = R^{+} \qquad 2.24$$

then, the interfering wave functions become,

$$\left\langle s'\middle| s''\right\rangle = \left\langle s\middle| R^2 \middle| s\right\rangle \qquad 2.25(a)$$

Averaging R^2 over the entire sphere, the interference term becomes,

$$\left\langle s\middle| R^2 \middle| s\right\rangle = -\frac{1}{2} \qquad 2.25(b)$$

$$P(r = 0, t) = \left|\sum_i A_i\right|^2 = \sum_i \left|A_i\right|^2 - A^2 \qquad 2.26$$

Thus, the phase induced by SOC decreases the return probability below its classical value (see Figure 2.2(b), resulting in destructive interference, this is known as WAL. In the next section, the effect of the magnetic field on the WL and WAL correction is discussed.

2.3.4 The Effect of the Magnetic Field on Localization Corrections

When an external magnetic field is applied perpendicular to the plane of the carrier motion, the trajectories will pick up an additional phase factor due to the magnetic vector potential, **A**. The additional phase factor is proportional to the magnetic flux through the area enclosed by the trajectory and is given by the line integral [49] for the clockwise trajectory as:

$$\frac{e}{\hbar c}\oint A.dl = \frac{e}{\hbar c}\int (\nabla \times A).dS \qquad 2.27$$

where **B** is given by: $\mathbf{B} = \nabla \times \mathbf{A}$

$$\frac{e}{\hbar c}\int (\nabla \times A).dS = \frac{2\pi BS}{\Phi_o} = \frac{S}{L_m^2} \qquad 2.28$$

where, S is the area enclosed by the trajectory and Φ_o =h/e is the flux quantum.

Then the total phase of the clockwise path is:

$$\varphi = k.r - Et/\hbar \rightarrow \varphi + \frac{e}{\hbar c}\oint A.dl$$

$$\rightarrow \varphi + \frac{2\pi BS}{\Phi_o} \qquad 2.29$$

where, $L_m \left(=\sqrt{\hbar/eB}\right)$is the magnetic length.

Since, the time reversed trajectories have the same path, but one traveled in opposite directions, the phases introduced by the perpendicular field are opposite in sign and the clockwise and counter-clockwise trajectories become:

$$A_{cw} \rightarrow A_{ccw} e^{2\pi SB/\Phi_o} \qquad 2.30$$

$$A_{ccw} \rightarrow A_{ccw} e^{-2\pi SB/\Phi_o} \qquad 2.31$$

Then, the total probability to return to the starting point in the presence of an external magnetic field is:

Weak localization

$$P(r=0,t) = \left|\sum_i A_i\right|^2 = 2A^2\left(1+\cos\frac{4\pi SB}{\Phi_o}\right) \qquad 2.32$$

Weak anti – localization

$$P(r=0,t) = \left|\sum_i A_i\right|^2 = 2A^2\left(1-\frac{1}{2}\cos\frac{4\pi SB}{\Phi_0}\right)$$

For Hall bar (HB) and wire devices, there are a large number of closed loop pairs. Their enclosed areas are different and random, consequently, each of the closed

loop pairs encloses different amount of magnetic flux (=SB) which cause a cutoff of the oscillatory cosine function. As long as the phase difference, $\delta\varphi=4\pi SB/\Phi_o$, is small, there is no significant effect on P(r=0,t) and as a consequence, the conductivity of the system is not altered. However, when $B > \Phi_o/4\pi S$, $\delta\varphi$ is large, the probability of returning to the origin is diminished, hence, a magnetic field reduces the quantum correction. When $B=\Phi_o/4\pi S$, the phase increment between two collisions becomes of order of unity and the magnetic field has a significant effect on the quantum correction. The time to accumulate a unit phase shift is called the magnetic relaxation time, τ_B. In the next section, theoretical models for WAL are discussed.

2.4 Theoretical Modeling of the Quantum Correction to the Conductivity in Low Dimensional Systems

WAL has different forms depending on whether the system is in the diffusive ($L_e<L_m$) or ballistic (($L_e>L_m$) regimes. In the diffusive regime, the quantum correction due to WAL for a low dimensional system in a perpendicular B has following form [5, 6]:

$$\Delta\sigma = \frac{G_0}{2}\left[\sum_{m=-1,0,1} F\left(\frac{H_\Phi}{B},\frac{H_{so}}{B}\right) - \sum_{m=0} F\left(\frac{H_\Phi}{B}\right)\right] \qquad 2.33$$

Where, $G_o = e^2/2\pi^2\hbar$ and H_Φ and H_{so} are the phase breaking and spin relaxation fields, respectively. The effective fields are scaled representations of SO and

phase coherence times ($H_{\Phi,s0} = (\hbar/4eD)1/\tau_{\Phi,so}$), so that they can be compared to the applied external field (B). The function $F(H_i,/B)$s defined in expression 2.33 are Cooperon channels, describing the interference contribution of scattered waves. The first term is the triplet (**S**=1), and the second term is the singlet (**S**=0). The terms have opposite signs. The triplet with **S**=1 enhances the conductivity (WAL) whereas the singlet **S**=0 contributes localization (WL) as expected for the spin-less limit. The phase breaking and spin relaxation fields determine the amplitude and the width of the WAL peak respectively. In the following sub-sections, theoretical models for the WAL are discussed.

2.4.1 Theoretical Model for the 2D Electron System

Over the last two decades, several theories of WAL which take into account both cubic and linear SOCs and which extend the model beyond the diffusive approximation have been developed. The first analytical model for WAL analysis was the Hikami-Larkin-Nagaoka model (HLN) [4], which considered the Elliot-Yaffet mechanism for electron spin relaxation. After the HLN model, more complex modifications were made, e.g., the Iordanskii-Lyanda-Pikus model (ILP) [5], the Pikus-Pikus model [8], the Lyanda-Geller ballistic model [6] and the Golub model covering both diffusive and ballistic transport [7]. These more involved models take into account both Rashba and Dresselhaus SOIs. Typically these modes can only address one linear mechanism at a time hence only one of the linear mechanisms (the Rashba or linear Dresselhaus) can be included in the

analysis. In symmetric QWs, the only SOI is Dresselhaus, thus, the ILP (S. V. **I**ordanskii, Yu. B. **L**yanda-Geller, and G. E. **P**ikus) model is sufficient to extract the SO and spin dephasing parameters of the 2D symmetric InSb/AlInSb QW described in chapter 5.

In the ILP model, the conductivity correction is expressed in terms of the Cooperon expression as:

$$\Delta\sigma(B) = \frac{-me^2\tau_o^2\delta}{4\pi^2\hbar}\sum_{\alpha\beta\eta\varsigma} C_{\alpha\beta\eta\varsigma}(n)$$

in which

$$\delta = \frac{4eBD}{\hbar c} \qquad 2.34(a)$$

$$C_{\alpha,\beta,\eta,\varsigma} = \frac{m}{4\pi^2\tau_o}\sum_r \frac{1}{E_{r,n}}\psi_{r,n}(\alpha,\beta)\psi^*_{r,n}(\eta,\xi)$$

The Cooperon represents a series of perturbation terms when spin up electrons with momentum **k** interact with spin down electrons with momentum – **k.** The amplitude of the cooperon, $C_{\alpha\beta\eta\zeta}$, depends on spin indices (α,β,,ζ). Where, $E_{r,n}$ and $\psi_{r,n}$ are the eigen values and eigen functions of the SO Hamiltonian for the 2D electron system, respectively. The Cooperon amplitude has been solved by perturbation theory for the singlet and triplet terms. In this model, the simplified conductance correction ($\Delta\sigma$ (B)) is:

$$a_n = n + \frac{1}{2} + \frac{H_\varphi}{B} + \frac{H_{so}}{B}$$

$$\Delta\sigma(B) = \frac{-e^2}{4\pi^2\hbar}\left\{\begin{array}{l} \dfrac{1}{a_0} + \dfrac{2a_0 + 1 + \left(\dfrac{H_{so}}{B}\right)}{a_1\left[a_0 + \left(\dfrac{H_{so}}{B}\right)\right] - \left(\dfrac{2H'_{so}}{B}\right)} + 3C + 2\ell n\left(\dfrac{H_{tr}}{B}\right) + \psi\left(\dfrac{1}{2} + \dfrac{H_\Phi}{B}\right) \\ -\displaystyle\sum_{n=1}^{\infty}\left[\frac{3}{n} - \frac{3a_n^2 + 2a_n\left(\dfrac{H_{so}}{B}\right) - 1 - 2(2n+1)\left(\dfrac{H'_{so}}{B}\right)}{\left[a_n + \left(\dfrac{H_{so}}{B}\right)\right]a_{n-1}a_{n+1} - 2\left(\dfrac{H'_{so}}{B}\right)\left[(2n+1)a_n - 1\right]}\right] \end{array}\right\}$$

2.34(b)

where Ψ is the digamma function, e is the electron charge, B is the applied magnetic field perpendicular to the 2D layer, and

$$H_{so} = \frac{\hbar}{4eD}\left(2\Omega_{D,\theta}^2\tau_1 + 2\Omega_{D,3\theta}^2\tau_3\right) \qquad 2.35$$

$$H'_{so} = \frac{\hbar}{4eD}\left(2\Omega_{D,\theta}^2\tau_1\right) \qquad 2.36$$

$$H_{tr,so,\Phi} = \frac{\hbar}{4eD}\frac{1}{\tau_{e,so,\Phi}} \qquad 2.37$$

H_{tr}, H'_{so} H_{so} and H_ϕ are parameterized magnetic fields. H_{tr} and H_Φ are related to the momentum and the inelastic relaxation times, H_Φ is known as the phase breaking field, because inelastic scattering events result in the loss of phase

memory. H'_{so} and H_{so} are related to the spin relaxation times. H'_{so}, H_{so} and H_{Φ} are the three fitting parameters. The phase coherence and spin relaxation time are related to their corresponding lengths by the diffusion constant $D = v_F^2 \tau / 2$,($L_{\varphi,so} = (D\tau_{\varphi,so})^{1/2}$). C is the Euler constant, n is the Landau level of the wave function and $\Omega_{D,\theta} = (\gamma k_F/\hbar)(\langle k_z^2 \rangle - k_F/4)$ and $\Omega_{D,3\theta} = (\gamma/\hbar)(k_F^3/4)$ are the Dresselhaus spin precession frequencies related with first and third Fourier harmonic of θ. The times τ_1 and τ_3 associated with probability of scattering by an angle θ in the 2D plane [5, 51].

$$\frac{1}{\tau_n} = \int W(\theta(\theta) - \cos(n\theta) d\theta \qquad 2.38$$

where, θ is the angle between k and the [100] axis, and $W(\theta)$ is the probability distribution function of the scattering by an angle θ. For n=1, τ_1 is the momentum scattering time (τ_e). Generally, the ratio between τ_3 and τ_1 evaluated the relative contribution of large and small angle scattering events. For isotropic scattering, $(\tau_1/\tau_3)=1$ and for small angle scattering $(\tau_1/\tau_3) = 9$. The 2D WAL data in chapter 5 were analyzed using this conductivity correction. The ILP model is valid in the diffusive regime only, i.e., for $L_e << L_m$. $L_m = \sqrt{h/eB}$ is the magnetic length and L_e is mean free path. This model can be applied to either the linear Rashba or Dresselhaus dominated 2D electron system.

2.4.2 Theoretical Model for the 2D Hole System

For 2D electron systems, it is assumed that the spin relaxation time is comparable to the phase breaking time, and that both are much longer than the momentum relaxation time. For hole systems, this is not the case. The mixing of the HH and LH bands depend on the carrier concentration and width of the QW, and as a consequence, the momentum and spin relaxation times can be comparable. To deal with this Averkiev *et al.* developed a new expression for the conductance correction for hole systems when one subband is occupied. In the AGP (N. S. **A**verkiev, L. E. **G**olub, and G. E. **P**ikus) model, the conductivity correction is expressed in terms of the Cooperon expression as [52]:

$$\Delta\sigma = \frac{e^2}{\pi\hbar}\int \frac{d^2q}{4\pi^2}A(q) \qquad 2.39(a)$$

Where A(q) describes the intensity of the interference of waves travelling through the closed loop in the opposite directions (Cooperon) and q is the momentum of both scattering waves. SOI of the p type 2D system are very strong, thus the Cooperon expression in this model has been solved perturbatively (non-perturbation). In this model, the Cooperon expression depends on the spin state and the quantized levels or subbands. For the case of a symmetric QW when only one subband is occupied, the expression A(q) is [52],

$$A(q) = [s(q) - 2p_1(q) - p_o(q)]\frac{2\pi ND\tau^2}{\hbar} \qquad 2.39(b)$$

The quantities s(q) and $p_{1,0}(q)$ describe the energy gaps between the HH and LH bands, Δ and Fermi energy, E_F.

In the limit $E_F << \Delta$, then $p_1=p_o$ and both quantities s(q) and p(q) are given by Ref. [52] as:

$$s(q) = \frac{\hbar}{2\pi\pi_0 D_o \tau_e^2} \frac{1}{q^2 + (D_o \tau_\Phi)^{-1}}$$

$$p_{1,0}(q) = \frac{\hbar}{2\pi\pi_0 D_o \tau_e^2} \frac{1}{q^2 + D_o^{-1}\left(\frac{1}{\tau_\Phi} + \frac{1}{\tau_{\perp,II}}\right)} \qquad 2.39(c)$$

Here, D and N are the diffusion constant and density of states at the Fermi energy calculated without considering the mixing of the HH and LH bands. τ_{II} and $\tau_\perp$ are the spin relaxation times directed along and perpendicular to the QW axis and τ_Φ is the phase relation time. In this model, the simplified conductance correction ($\Delta\sigma(B)$) for hole systems with one occupied subband has the following form:

$$\sigma(B) - \sigma(B=0) = \frac{e^2}{\pi h}\left[\begin{array}{l} \psi\left(\frac{1}{2} + \frac{H_\varphi + H_{II}}{B}\right) + \frac{1}{2}\psi\left(\frac{1}{2} + \frac{H_\varphi + H_\perp}{H}\right) - \psi\left(\frac{1}{2} + \frac{H_\varphi}{H}\right) \\ \\ + \ell n\left(\frac{H}{H_\varphi + H_{II}}\right) + \frac{1}{2}\ell n\left(\frac{H}{H_\varphi + H_\perp}\right) - \ell n\left(\frac{H}{H_\varphi}\right) \end{array}\right] \qquad 2.39(d)$$

in which,

$$H_{II,\perp,\varphi} = \frac{\hbar}{4\pi\pi}\frac{1}{\tau_{II,\perp,\varphi}} \quad \text{as usual.} \qquad 2.40$$

Once again there are three characteristic magnetic fields, $H_{\shortparallel}$, $H_{\perp}$ and H_{φ}. $H_{\shortparallel}$ and $H_{\perp}$ are the spin relaxation fields directed along and perpendicular to the QW axis respectively. The ratio of $H_{II,\perp}/H_{tr}$ indicates the degree of mixing between the HH and LH bands.

$$\frac{H_{II}}{H_{tr}} \sim \left(\frac{E_F}{\Delta_{HL}}\right)^2 \qquad 2.41$$

$$\frac{H_{\perp}}{H_{tr}} \sim \left(\frac{E_F}{\Delta_{HL}}\right)^3$$

Where, Δ_{HL} is the minimum separation between HH and LH energy bands. At low densities, where $E_F/\Delta_{HL} << 1$ the band mixing is weak and both $H_{\shortparallel}$ and $H_{\perp}$ are smaller than H_{tr} (H_{II} and $H_{\perp} << H_{tr}$). At high densities, where, $E_F/\Delta_{HL} \approx 1$, the band mixing is strong and then, H_{II} and $H_{\perp}$ are comparable to H_{tr}, (H_{II} an $H_{\perp} \approx H_{tr}$). The WAL data in chapter 6 were analyzed using this conductivity correction.

2.4.3 Suppression of Spin Relaxation in the 1D Electron System

Several theoretical investigations for the 1D system have shown that the spin relaxation length can be significantly enhanced by controlling the geometric width when it is smaller than the 2D bulk spin precession length (L_{so}) [53-55]. In the 2D case, the channel width is greater than the bulk spin precession length, and the relevant area for a time-reversed path to result in a π spin rotation is proportional to the spin relaxation time.

$$L_{so}^2 \approx D\tau_s \qquad \text{(for 2D case)} \qquad 2.42$$

As the channel is narrowed, L_{so} will eventually exceed the channel width, and the relevant area, $L_{so}^2(W)$ becomes proportional to $WL_{so}(W)$ instead. Like the 2D case, $L_{so}^2(W)$ is proportional to a spin relaxation time,

$$D\tau_s(W) \approx WL_{so}(W) \approx L_{so}^2$$

$$\text{(for 1D case)} \qquad 2.43$$

$$L_{so}(W) \approx \frac{L_{so}^2}{W}$$

Where L_{so} is the width independent 2D limit and $L_{so}(W)$ is the quasi-1D analog. This implies the $L_{so}(W)$ grows with decreasing wire width in the 1D case. Subsequent to theoretical prediction of this dimensional confinement effect, the idea was experimentally investigated and confirmed by several groups for various material systems, e.g., InGaAs/InP, InAs, InSb and AlGaN/GaN via transport and optical experiments [20, 21, 56-60] (see Figure 2.4).

By considering this dimensional confinement effect, the expression for the SO field in the 1D limit was derived by Ketterman [53]:

$$H_{so}(W) = \frac{\pi^2}{3}\left(\frac{W}{L_{so}}\right)^2 H_s(2D) \qquad 2.44$$

As a consequence, in a narrow channel the spin relaxation length can be enhanced without changing the SOC (see Figure 2.4). The suppression only applies for linear SOC terms; higher order terms are unaffected. For systems in which both the linear and cubic Dresselhaus interaction are relevant, the spin relaxation can be anisotropic, see Figure 1.3b. Typically the cubic Dresselhaus is weak along the [100] direction and strong along [110] (see Figure 1.3b).

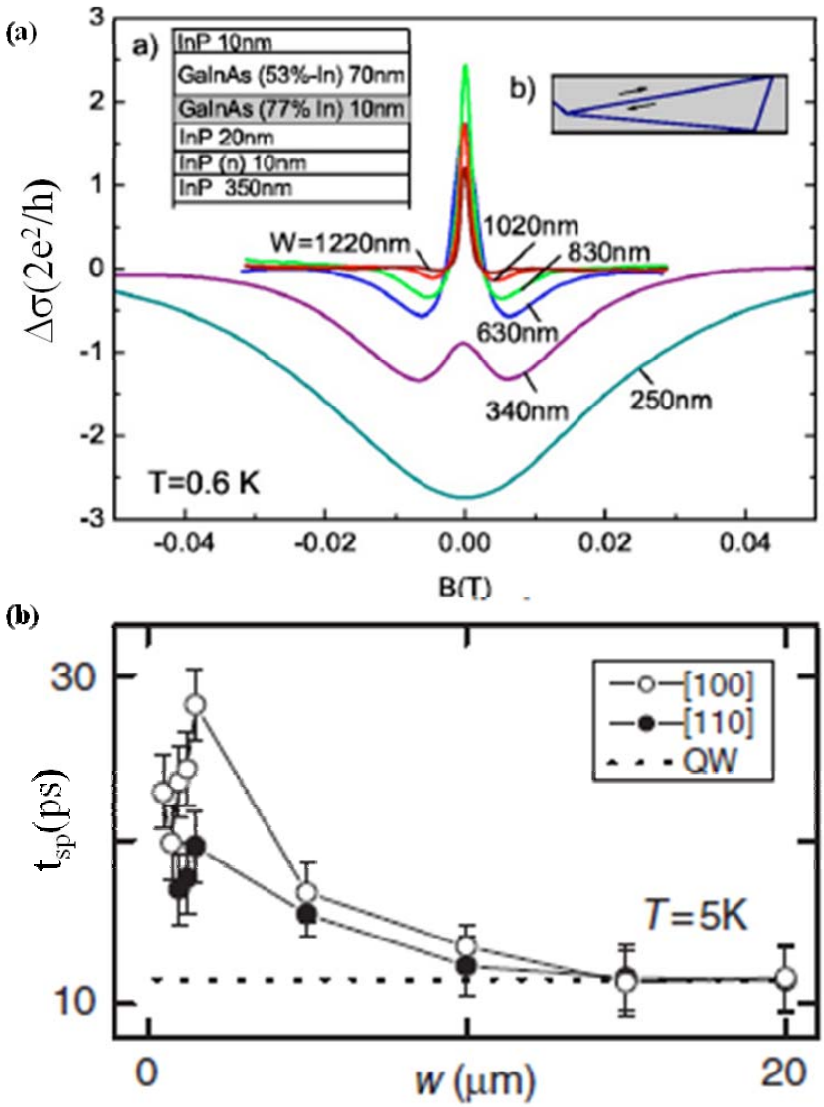

Figure 2.4 (a) The magneto-conductivity corrections for the various wire widths at 0.6K This figure is taken from Ref. [20]. (b) The width dependence of spin relaxation times for the [100] and [110] directions. Spin life time along the [110] direction is shorter than the spin life time along the [100] direction. This figure is taken from Ref. [21].

This anisotropic effect is not observable in 2D heterostructures, however for 1D wires fabricated along different crystalline directions, the anisotropy spin relaxation was been observed by Holleitner *et al*. for InGaAs QWs via an optical

technique [21] (see Figure 2.4(b)). Chapter V details a transport measurement of this anisotropy.

2.4.4 Theoretical Model for 1D Electron System

Chapter V of this thesis deals with quantum wires, where it is important to modify the 2D ILP model for the quasi-1D limit where the channel width $W<<L_{so}$. In addition to changes in the spin relaxation length for 1D wires described in section 2.4.3, the magnetic length in a 1D system also behaves differently than in 2D. In 2D, the area to enclose a flux quantum is $S\sim L_B^2\sim D\tau_B$. When the magnetic length exceeds the channel width in the diffusive regime ($L_e<<W$), Beenakker *et al.* have shown that the relevant area is $S \sim W (D\tau_B)^{1/2}$ [61,62]. In both cases, $L_e<<W$, thus transport is diffusive.

Then in quasi-1D, there is a width dependent magnetic length.

$$L_B(W) = \sqrt{D\tau_B} \sim \frac{L_m^2}{W} \qquad \text{1D case} \qquad 2.45$$

Al'tshuler and Aronov calculate a similar time scale, τ_B (W), for thin films isgiven by:

$$\tau_B = \frac{3\hbar^2}{De^2W^2B^2} = \frac{3L_m^4}{Dw^2} \qquad 2.46$$

By considering the effects of channel width, Beenakker and Van Houten have developed a WAL expression for a quasi-1D system in the diffusive limit, i.e., L_e<W. with the quantum conductance correction given by expression [49]:

$$\Delta\sigma(B) = -\frac{e^2}{hL}\left[2\left(\frac{1}{L_\varphi^2}-\frac{1}{2L_s^2}+\frac{1}{L_B^2}\right)^{-1/2}+\left(\frac{1}{L_\varphi^2}-\frac{1}{L_s^2}+\frac{1}{L_B^2}\right)^{-1/2}-\left(\frac{1}{L_\varphi^2}+\frac{1}{L_B^2}\right)^{-1/2}\right] \quad 2.47$$

where, L is the length of the wire and L_B is the dimensional crossover magnetic length between 2D case (L_m<W) and 1D case (L_m>W).

At the crossover,

$$\begin{aligned}\tau_B(\text{crossover}) &= \tau_B(\text{strong field}) + \tau_B(\text{weak field}) \\ &= \tau_m + \tau_B(W)\end{aligned} \quad 2.48$$

Then,

$$L_B(\text{crossover}) = \sqrt{L_m + L_B(W)} \quad 2.49$$

$$L_B(\text{crossover}) = L_m\sqrt{1+3\frac{L_m^2}{W^2}}$$

Using this quasi-1D model, width dependent spin relaxation lengths (L_{so}(W)) for 1D InSb wires were extracted for the experiment described in chapter 5. Fitting programmers for all these WAL expressions (2D and 1D) were written in Mathematica 6.0 using non-linear regression.

Chapter 3: Device Fabrication Technology

3.1 Introduction

Two transport experiments are described in this thesis. Both were performed on a 2DEG/2DHG, hosted in an InSb/AlInSb heterostructure. Before describing the experimental results, a brief description of device processing techniques involved in the InSb sample fabrication will be given in this chapter. There are several techniques for this device fabrication which are: lithography; etching; contact processing and annealing; and wire bonding. This chapter begins with lithography followed by the other techniques.

3.2 Lithography

Optical lithography and electron beam lithography (EBL) are the two standard lithography techniques to transfer a geometric pattern onto the surface of the sample. Both techniques involve the use of the resists (photon or EB sensitive resists), which are usually organic polymers whose chemical bonds can be changed by exposure to radiation. For this thesis work, both lithography techniques were used for device fabrication.

3.2.1 Photolithography

Photolithography is a process used in micron-size and larger fabrication. It uses light sensitive resists to transfer a photo mask pattern onto the surface of the sample. There are several steps involved for the photolithographic process. All the

photolithographic steps must be done in the cleanroom to avoid dust and small particle contamination. The first step of the sample processing is scribing a typically 8x8 mm square piece of the semiconductor wafer by using a scriber. Then the surface of the sample is rinsed with appropriate solvents, a sequence of acetone, methanol, and isopropanol to remove the dust from scribing, cleaving, and photo resist residue from any previous photolithography processing and blown dry after each solvent using filtered nitrogen gas. After pre-cleaning, the sample was baked in a conventional oven at 150 C^{o} and 15 min in order to evaporate any residual solvent, and then coated with AZ5124A resist spun on at 4000 RPM and 40 seconds for a final resist thickness of 1.4m -1.5micron thick (see Figure 3.1).

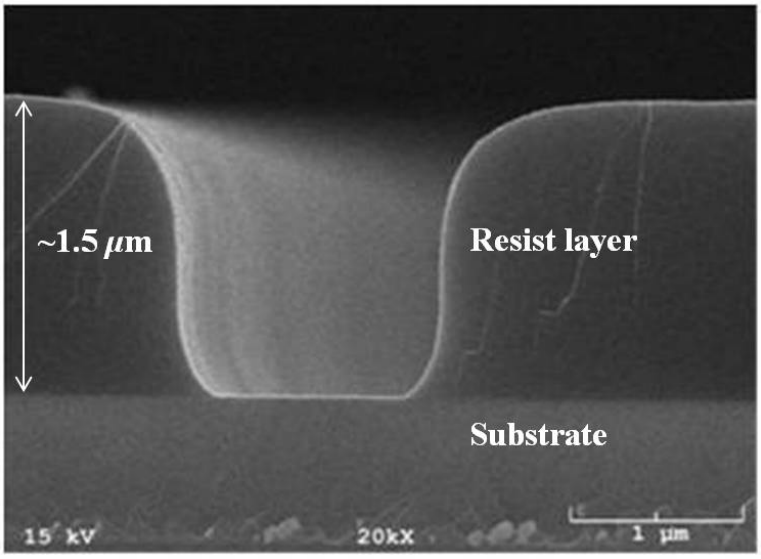

Figure 3.1 A scanning electron microscope (SEM) cross-sectional image of the AZ512E resist profile after development in MIF 319 developer solution for 60s. This was imaged with a JOEL 880 SEM after sputtering on a thin ~ 2nm Ir layer.

After spin coating, the sample was soft-baked at 95°C and 60 seconds on a hot plate to get rid of excess resist solvent and to promote a solid resist layer. The sample was then exposed using a Karl Suss MJB3 mask aligner and developed with MIF 319. Figure 3.2 shows the basic lithography fabrication sequences for positive and negative steps.

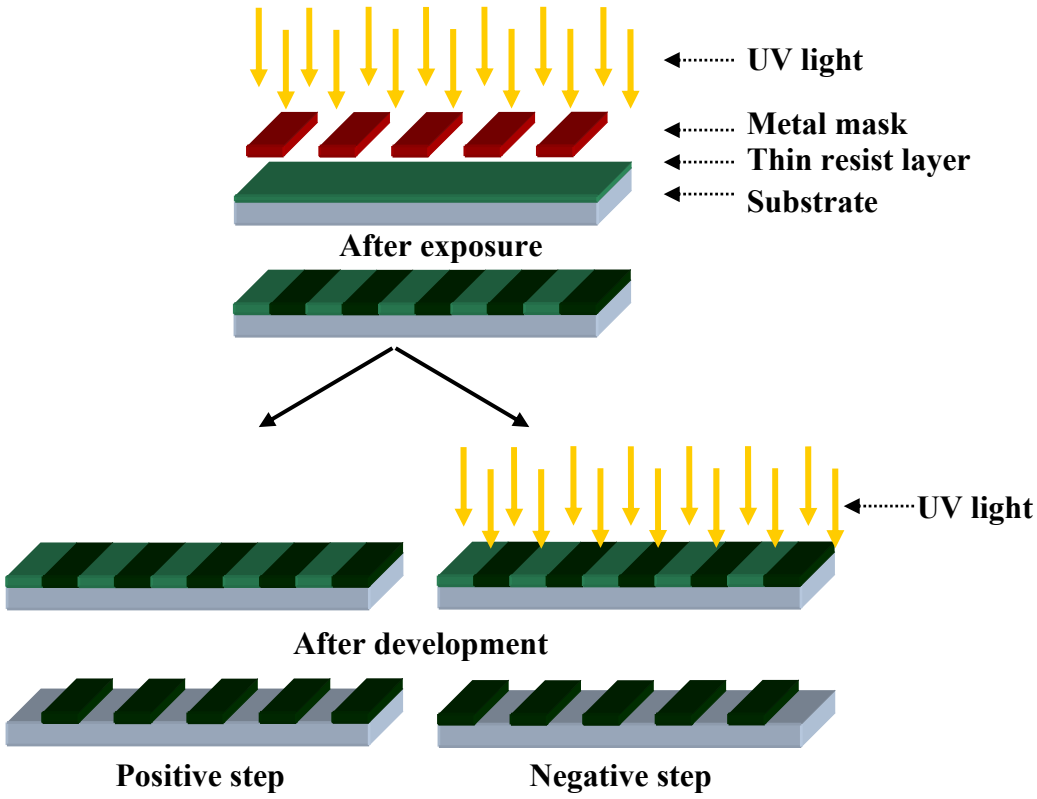

Figure 3.2 Basic lithography fabrication sequences (not to scale): (a) Positive step. (b) Negative step.

AZ512E is a reversing resist allowing both positive and negative patterning. Positive patterning was used for the mesa etch, while negative patterning was used for the contacts. For the positive step, there was a single light exposure of 60 seconds, whereas the pattern can be reversed by removing the mask and doing a

second blanketing exposure to the UV radiation for 60 seconds. After exposure, the undeveloped resist layer was hard-baked on a hot plate at 120^{o}C for 60 seconds. MIF 319 is the common developer for either positive or negative processes. Images of the photo mask of the mesas are displayed in Figure 3.3. Additional details of the photo lithography recipe for InSb can be found in Appendix A. For the negative contact step, a thin layer of pure Indium (for n-type heterostructures) or InZn (95% In and 5% Zn) alloy (for p-type heterostructures) was thermally evaporated followed by a lift-off of the unexposed resist using 1165 resist remover solution. Contacts were then annealed at 230 ^{o}C for five minutes in forming gas to establish ohmic contacts. The etching process which followed positive exposure is described below.

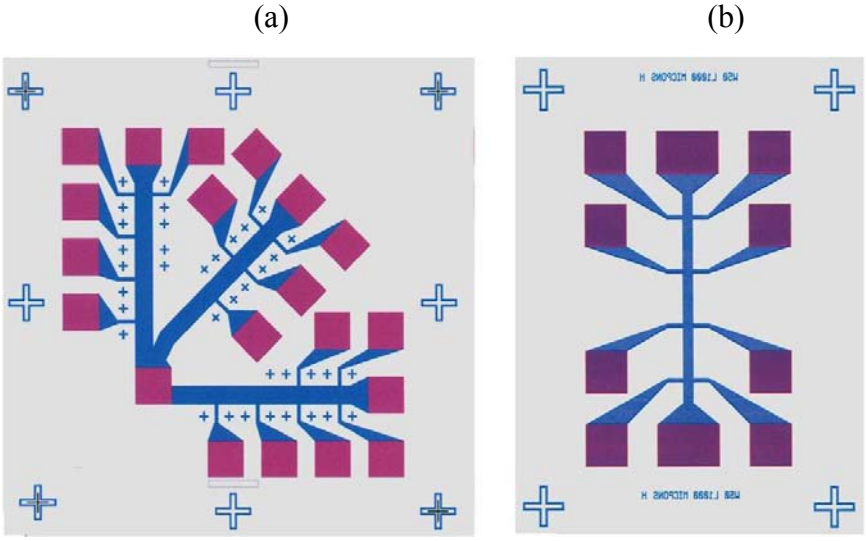

Figure 3.3 Photo mask used for photo lithography exposure (a) HB mesa for 1D wire fabrication project. The total structure size is ~2x2 mm^2. (b) HB mesa for 2DHG project. The single structure size is ~2x1.2 mm^2. Large crosses that separated the HB arrays were used as photo-lithography alignment marks and small crosses either sides of the channel width were used as EBL alignment marks.

3.2.2 Electron Beam Lithography (EBL)

The Suss MBJ-3 mask aligner resolution (≈ 2 micron resolution) is insufficient for 1D wire fabrication for the quantum interference experiment, thus EBL was also employed which is widely used for creating patterns in the sub-micron size range. The EBL procedure is very similar to photolithography with the principal differences being the source and exposure. In EBL, the source is an energetic EB instead of UV light, and the patterning is achieved through direct writing instead a single UV light dose through a mask.

Our EB pattern design was done using Design CAD. The important part of the microscope is an EB column, containing an electron gun, magnetic lenses, and a specimen chamber. The electron gun provides free electrons which are accelerated towards the sample by an electrostatic field.

The EB work in this thesis was performed using a JOEL 840 SEM, with an electrostatic beam-blanker. The beam source was either a tungsten (W) or LB_6 filament The EBL patterns followed the annealing of the in contacts. The HB mesa was coated with ZEP520 resist spun on at 5000 RPM for 45 seconds to obtain a ~500nm thick uniform resist layer, then pre-baked at 170^{o}C for 3 minutes on a hot plate to evaporate away excess EB resist solvents. After the sample was loaded into the microscope stage, the beam current was measured by focusing the EB into a Faraday cup and was adjusted to 10pA. Next the beam was focused onto the resist using the general JOEL 840 SEM procedure for a 40keV EB. After

achieving good focus at 300kx magnification, the resist was exposed scanned using the deflection coils in the SEM and the Nabitty control system.

Exposure and development times had already been optimized by means of dose tests. Our dose test pattern was an array of boxes with a write field usually set as 500 μm x 500 μm. Each array element consisted of 10 identical boxes (box: 500 nm x 10,000 nm, 5 boxes separated by 500nm and 5 boxes separated by 1000nm). Each element was exposed using a slightly different dose by point exposure time. Separate samples were developed in xylenes for different times, thus we could optimize both dose and development in a single experiment. Results of these dose and development time tests are summarized in Figures 3.4 and 3.5. The optimal area dose was ~90 μC/cm^2.

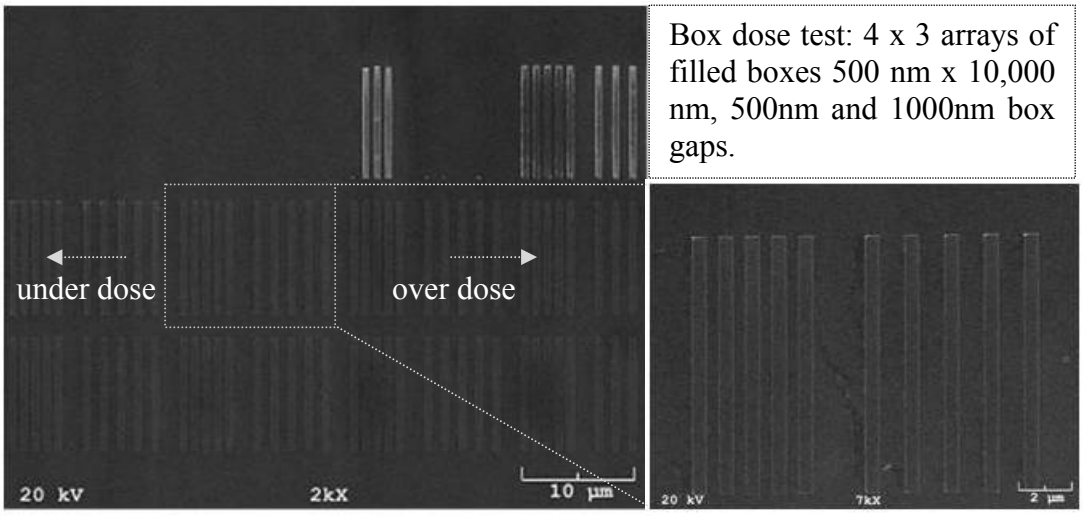

Figure 3.4 Area dose test for ZEP520 EB resist developed for 45 seconds. Images were taken by a JOEL 840 SEM. The minimum dose ~40μC/cm^2, while the maximum dose ~160 μC/cm^2 with a step size ~10 μC/cm^2. The array exposed at the optimal dose is shown in the inset.

As can be seen in the SEM images for the 30 second development time, the pattern was transferred but left undeveloped resist at the sidewalls. Increasing to 50 seconds, the resist was over developed and a huge undercut can be seen. At 45 seconds, patterns were well transferred and sidewall undercutting was minimal.

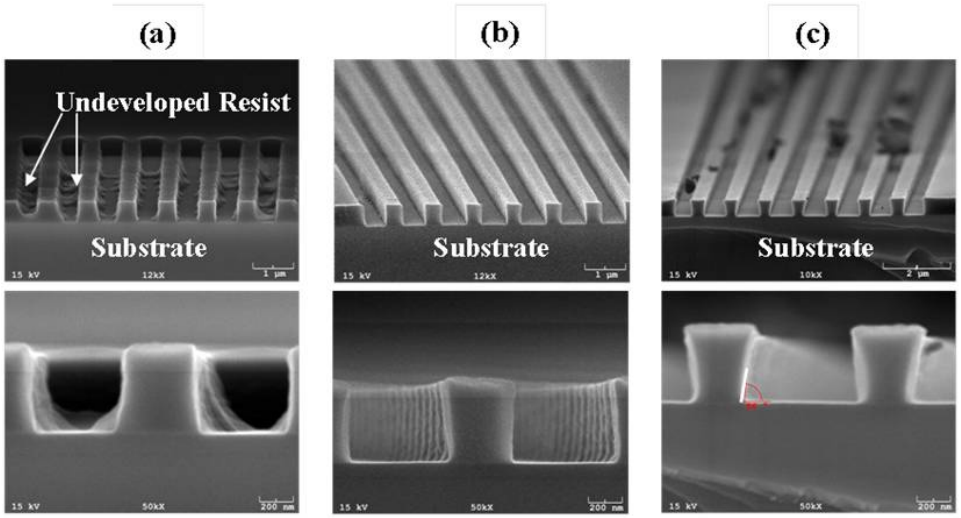

Figure 3.5 Cross section SEM images from the JOEL 880 of the 500 nm wires after development for 30 seconds (b) 45seconds and (c) 50 seconds.

After exposure and development (see Appendix B for details), the sample was post-baked on a hot plate at 130^{o}C for 60 seconds to evaporate excess DI water and solidify undeveloped resist and then etched in a BCl_3/SF_6 based plasma (see details below). For wire fabrication, the write field was set at 300 μm x 300 μm to fabricate 200 μm long wires as described in chapter 4. Figure 3.6 shows the SEM images of the array of 500nm wide wires array. As can be seen in the images, the wires were uniform across a relatively wide region and throughout their length.

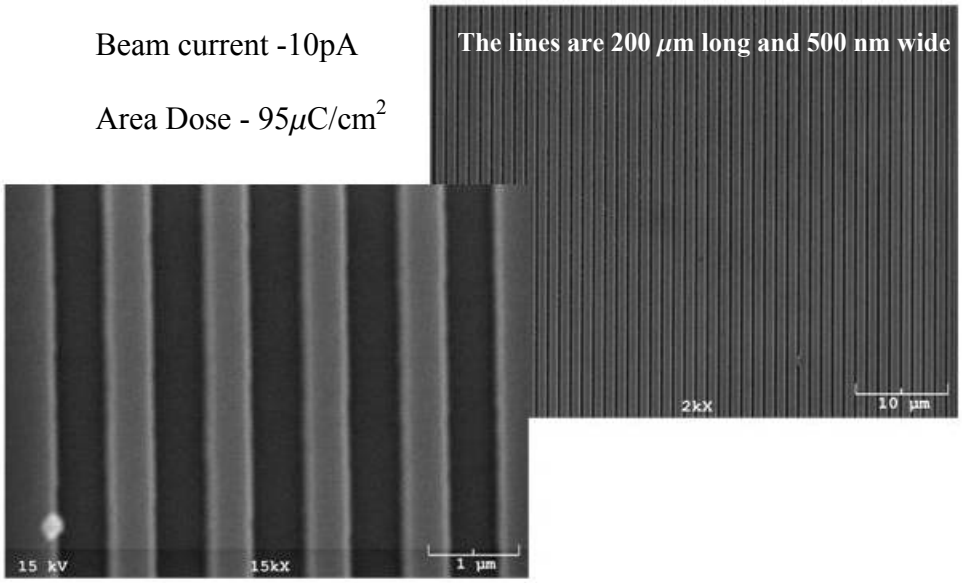

Figure 3.6 Top down view of the wire arrays. Images were taken from JOEL 840 SEM. The width of the wire is uniform throughout the length of the wire.

3.3 Etching

3.3.1 Wet Etching

Wet etching is the simplest etching technology as it is quick, easy and cheap, utilizing liquid chemicals to remove material. In general, the majority of wet etching solutions for semiconductors are mixtures of one or two acids with an oxidizer. The basic mechanism is the formation of an oxidized layer and subsequent dissolution by acids. Wet etching is generally isotropic, proceeding in all directions at the same rate and resulting in undercutting of the pattern to an extent equivalent to the etch depth. Thus, it is a good choice for micron sized features with shallow etches depth, such as Hall bar (HB) geometries on shallow QWs such as those studied in this thesis where the wells are buried 50nm below the surface.

For InSb/InAlSb, the wet etching solution was 3% H_2O_2 + 2.5% HF + 85% Lactic acid mixed at volume ratio of 6:3:1 respectively. The above solution gave an etch rate of ≈ 1020 nm/min. Etching was stopped by rinsing the sample in DI water for approximately three minutes. The photoresist was then dissolved in 1160 remover and the sample was rinsed in DI water and finally blown with dry N_2 gas before wire bonding (hole sample) or coating a second lithography step via EB to fabricate the 1D wires. Etch depths were taken from SEM studies of the depth wall profiles (see Figure 3.7).

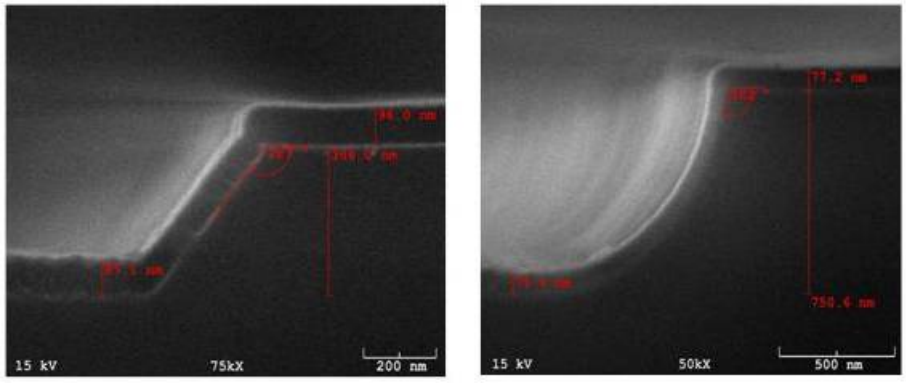

Figure 3.7 Wet etching depth profiles of the InSb/AlInSb heterostructure. These images were taken from JOEL 880 SEM after the resist was removed and on SiO_2 layer was deposited. (a) Shallow etching: wet etched for 25s. (b) Deep etching: wet etched for 45s. Shallow depth profile is more anisotropic than the isotropic expected from wet etching.

3.3.2 Dry Etching

Dry etching is widely used for sub-micron features, because unlike wet etching, it can provide nearly anisotropic etching with minimal mask undercutting. Several different dry etching processing systems are in use today. The dry etching

technique performed in this work used high density Inductively Coupled Plasma (ICP) with a parallel plate Reactive Ion Etching (RIE) system. This system generates the plasma between the electrodes at the standard frequency of 13.56 MHz in a system in which the gas flow rates, chamber pressure, RIE and ICP powers are separately controllable variables. Ion energy and current (plasma density) depend on RIE and ICP powers respectively.

This dissertation used an RIE process for InSb/AlInSb developed using BCl_3/SF_6 gas mixtures. According to the literature, BCl_3/SF_6 yields complex plasma chemistry, forming many possible species and resulting in many possible reactions. The BCl_3/SF_6 recipes were tested a function of ICP, and RIE, source powers at fixed flow rates of the gas species and chamber pressure, 12 to 9 sccm respectively for BCl_3 and SF_6 and 2mTorr overall pressure. Etch depths were measured by a profilometer after removing the resist. Figure 3.8 summarizes the etch rates of InSb/AlInSb as a function of the ratio RIE power to ICP power.

As the power ratio is increased, the etch rate of InSb/AlInSb first increases then decreases. This may be due to the competition between ion energy and plasma density. Sidewall profiles are studied by taking cross-sectional SEM images. Figure 3.9 shows the SEM micrographs for all the tested recipes. As can be seen, the etched surface was very smooth for all the tests of BCl_3/SF_6 and similar undercut control and anisotropic etching can be seen for the various power ratios.

With the exception RIE/ICP ≈ 2.75 the sidewall angles were approximately constant, and were measured as ≈ 40-45°.

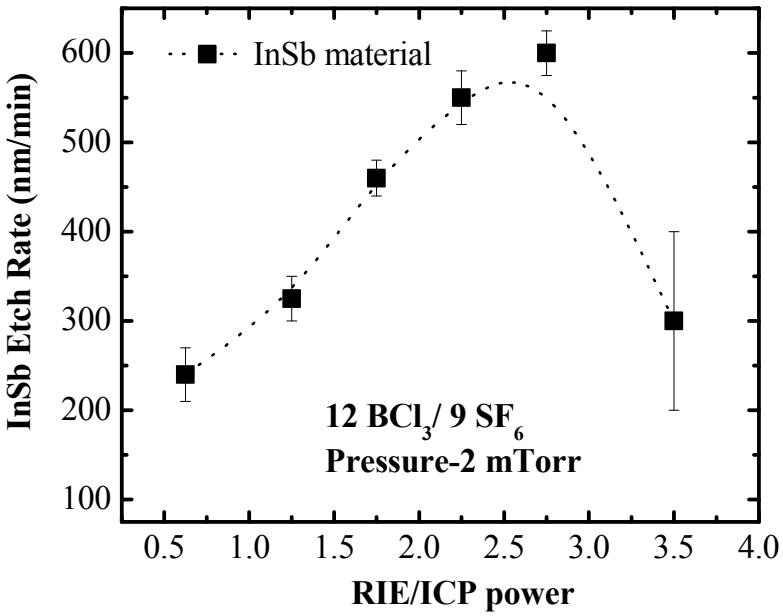

Figure 3.8 Etch rate of InSb/AlInSb as a function of the ratio of RIE power to ICP power. The operating chamber pressure and total gas flow (BCl_3+SF_6) were held constant at 2mTorr and 21sccm, respectively.

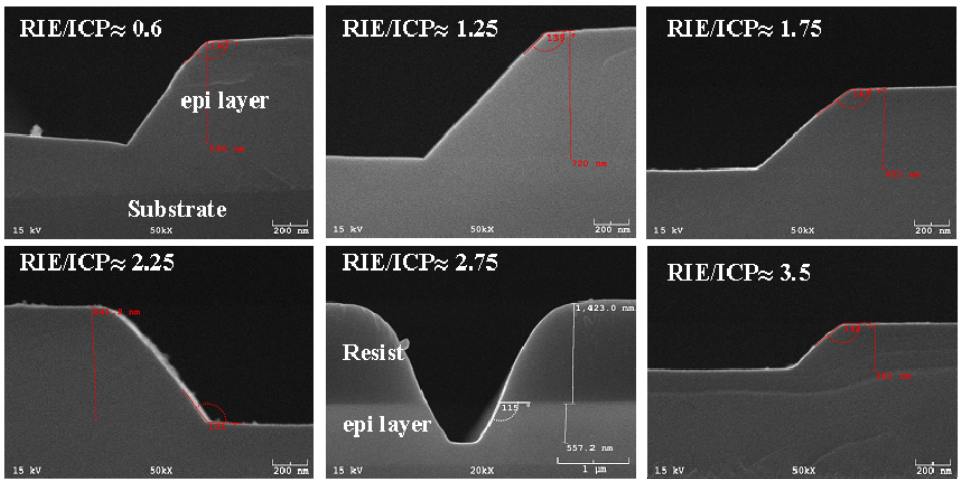

Figure 3.9 Sidewall profiles for dry etching recipes. The operating chamber pressure and total gas flow (BCl_3+SF_6) were held constant at 2mTorr and 21 sccm, respectively.

1D wire arrays fabricated on the top of the HB mesa for the transport experiment were finally etched using the following dry etching recipe:

ICP power- 200 W

RIE power- 550W

Chamber pressure- 2mTorr

BCl_6 : SF_6 gas mixture ratio- 12 sccm : 9 sccm

Following dry etching, the EB resist was removed in acetone and the sample rinsed in DI water and blown dry with N_2 before wire bonding was performed. Figure 3.10 shows the final 1D wire devices mounted on 28 pin PLCC wire bonded using K&S 4500 digital serial manual wedge bonder with high purity 25 μm thick gold wire. After wire bonding low field four-terminal magneto-transport measurements were performed in a ^{3}He cryostat system in perpendicular magnetic field at temperatures ranging from 10 to 1.5K.

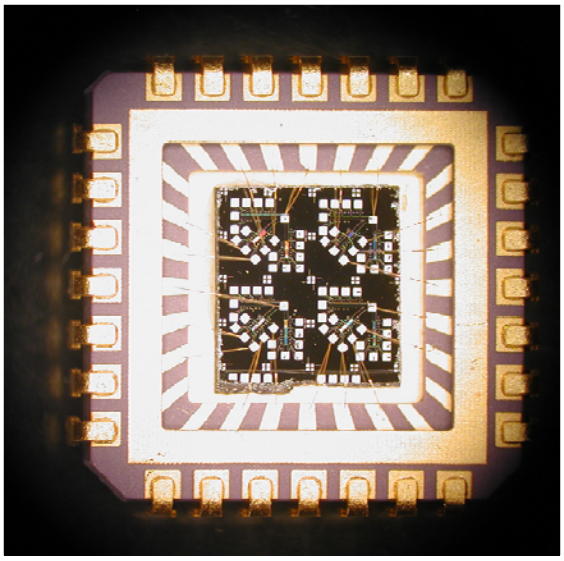

Figure 3.10 1D wire device mounted on 28 pin PLCC.

Chapter 4: InSb and Quantum Well Structures

4.1 Introduction

InSb is an III-V compound semiconductor which crystallizes in the zincblende structure. The zincblende structure consists of two interpenetrating face centered cubic (FCC) sub lattices. One sub lattice is made of the group III atoms (Ga, In and Al) and the other sub lattice is made of group V atoms (As, P and Sb). These two sub-lattices are displaced from each other by a distance (a/4, a/4, a/4) along the body diagonal. Thus, the zincblende structure does not have a center of inversion symmetry and this gives rise to spin splitting of the electron and hole states at non-zero wave vector even in the absence of external magnetic field.

Among the III-V semiconductors, InSb offers interesting material assets. It has the smallest electron effective mass, the highest g-factor, spin-orbit split off energy, and the strongest non-parabolic dispersion of the electrons and holes. Hence, these material assets are making InSb suitable for some spintronic applications and fundamental experiments to understand the spin properties of the narrow gap semiconductors. Room temperature values of some parameters for InSb, GaAs and InAs materials are listed in Table 4.1 for comparison.

The typical band structure of a bulk III-V semiconductor is shown in Figure 4.1(a). Generally, by sandwiching a thin layer of lower band gap material between two layers of higher band gap material, a type I QW channel is formed. The type I QW is the most widely studied heterostructures. It exhibits straddled band

alignment, i.e. the steps in the VB and CB go in the opposite direction as shown in Figure 4.2. At the interface, energies of the CB and VB edges (barrier height) change and their magnitudes depend on the barrier alloy composition.

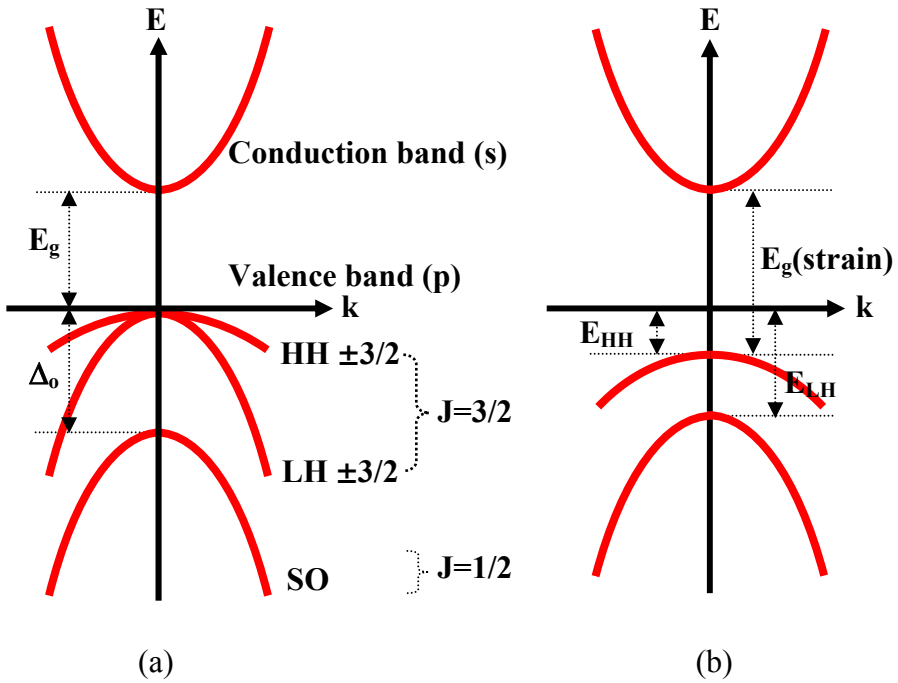

Figure 4.1 Band structure diagram of (a) bulk III-V and (b) III-V QW. E_{HH}, E_{LH} are the HH and LH band energies in the QW.

In QWs, the carriers can be trapped in a very narrow potential well confining the carriers in the z direction (growth direction), so that, the carriers are only free to move in the xy-plane. In the example, a type I QW is formed in an InSb layer between two AlInSb layers. Because it is a type I, the thin InSb layer acts as a well for both the CB and VB and the well is compressively strained because of the lattice mismatch between the InSb and AlInSb materials. The lattice constant of the $Al_xIn_{1-x}Sb$ can be calculated by [63],

$$a_{Al_xIn_{1-x}Sb} = a_{InSb}(1-x) + a_{AlSb}(x) \qquad 4.1$$

where, a_{InSb} and a_{AlSb} are the lattice constant parameters for bulk InSb and AlSb, 6.479 Å and 6.14 Å respectively. This strain has a significant effect on the effective mass of the hole. According to the VB dispersion relation in the Luttinger model, the effective masses of the HHs and LHs for the III-V materials are given by [14],

(a) direction of in-plane motion (xy-plane) are,

$$m^*_{HH} = \frac{m_0}{\gamma_1 + \gamma_2}$$

$$m^*_{LH} = \frac{m_0}{\gamma_1 - \gamma_2} \qquad 4.2(a)$$

(b) direction of quantization (z direction) are,

$$m^*_{HH} = \frac{m_0}{\gamma_1 - 2\gamma_2}$$

$$m^*_{LH} = \frac{m_0}{\gamma_1 + 2\gamma_2} \qquad 4.2(b)$$

Where m_o is the free electron mass and γ_1 and γ_2 are the Luttinger parameters for the material. These mass expressions yield the HH-LH band mixing at non-zero wave vector by neglecting all off-diagonal terms. According to the above effective mass expressions, in the xy-plane, the HH states have a lighter mass whereas the LH states have a heavier mass, however in the perpendicular

direction, this is reversed. As a result of the different effective hole masses, the HHs and LHs bands have different ground state energies, and the bands are separated at near k=0 as shown in Figure 4.1(b). The splitting of HH and LH states in the z direction (growth direction) is called the HH-LH splitting.

Table 4.1. Room temperature parameters of InSb, InAs, GaAs and AlAs [22].

Parameter	InSb	InAs	GaAs	AlAs
Energy gap (eV)	0.17	0.35	1.42	3.13
spin-orbit split off energy (eV)	0.81	0.38	0.34	0.30
Electron effective mass (m^*/m_o)	0.014	0.023	0.065	0.15
In-plane HH effective mass (m_{HH}^*/m_o)	0.019	0.27	0.12	0.26
In-plane LH effective mass (m_{LH}^*/m_o)	0.049	0.028	0.21	0.38
Out off-plane HH effective mass (m_{HH}^*/m_o)	0.244	0.035	0.38	0.51
Out off-plane LH effective mass (m_{LH}^*/m_o)	0.014	0.083	0.09	0.22
Electron g factor	-51.56	-14.9	-0.44	1.52
Dielectric constant (ϵ/ϵ_o)	16.8	15.1	12.9	10.0
Intrinsic mobility ($cm^2/v.s$)	77000	39000	9000	-
Lattice constant (Å)	6.479	6.058	5.653	5.66
Dresselhaus coefficient (eV $Å^3$)	760	27.18	27.58	18.3
γ_1	37.10	20.40	6.85	3.25
γ_2	16.50	8.30	2.10	0.65

In addition, compressive strain also causes an increase in the energy gap. For $InSb/Al_xIn_{1-x}Sb$ heterostructures, the effect of the strain on the energy gap has been experimentally shown in Refs. [63, 64] as:

$$E_g(\text{Strain}) = E_g + 0.157x_{\text{barrier}}(\text{eV}) \leftarrow (E_g \text{ for strained InSb at } \Gamma \text{ point})$$
$$E_g(\text{Strain Relaxed}) = E_g + 2.06x_{\text{barrier}}(\text{eV}) \leftarrow (E_g \text{ for unstrained AlInSb layer}) \quad 4.3$$

here, $x_{barrier}$ is the Al composition in the barriers on either side of the QW and E_g is the energy band gap of the unstrained InSb material. InSb is a direct band gap semiconductor, with a gap of about 0.24 eV at low temperature ($\approx$ 4K).

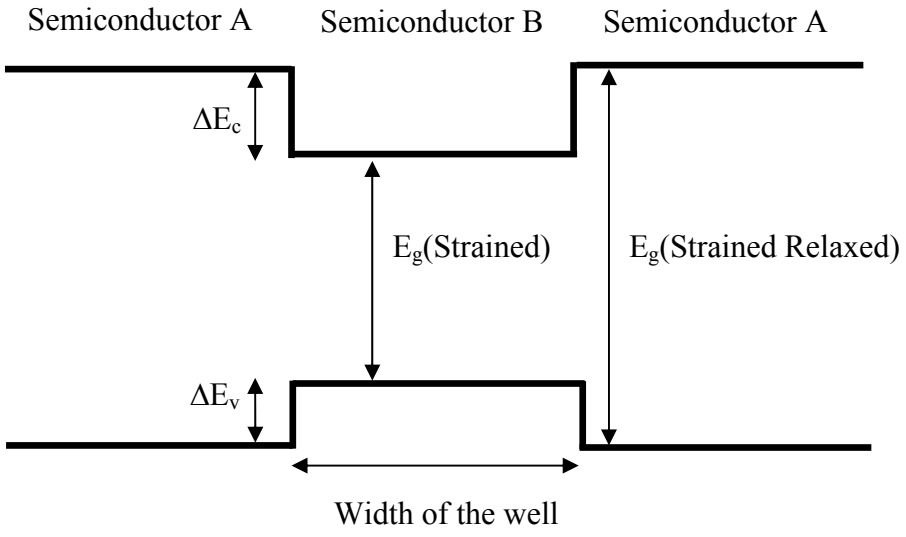

Figure 4.2 Type I QW channel.

The bands of narrow gap semiconductors like InSb are highly non-parabolic, thus, the effective mass is energy dependent. Kane has developed a six model that

includes the non-parabolic nature of the band. In his model, the energy dispersion for the CB and the VB is given as:

$$E\left(1+\frac{E}{E_g}\right)=\frac{\hbar^2 k^2}{2m^*} \tag{4.4}$$

where E is the energy of the electron and k is the wave vector. Then, the energy dependent effective mass, m(E) obtained as of the first deviation of the energy with respect of the wave vector is,

$$m(E)=m^*\left(1+\frac{2E}{E_g}\right) \tag{4.5}$$

When $E=E_F$, the Fermi energy for non-parabolic semiconductor is,

$$E_F=\left(\frac{E_g^2}{4}+\frac{\hbar^2 k_F^2 E_g}{2m_{xy}^*}\right)^{1/2}-\frac{E_g}{2} \tag{4.6}$$

Here, k_F is the Fermi wave vector. In the following section, the details of our InSb QW structures are given and their band parameters were calculated using above equations.

4.2 InSb Quantum Well Structures

Five Al_xIn_ySb/InSb heterostructures were used in this thesis work to investigate the SOI through transport. These five heterostructures were labeled as t340, t196, t198, t200 and t250. They were grown by molecular beam epitaxy (MBE) on a

semi-insulating (001) GaAs substrate. Figure 4.3 shows the examples of the layer sequences for t340 and t196 QW structures grown by MBE. The quantum confinement in the wells was obtained using $Al_{0.20}In_{0.80}Sb$ spacer layers. Carriers are provided to the well by the remotely δ-doped layers which can be either on both sides or on one side of the QW, resulting in symmetric and asymmetric wells respectively. For all structures, the QW was only 60 nm below the surface forming a shallow QW. In each structure, an additional δ-doping layer was placed a distance y nm below the $Al_{0.10}In_{0.90}Sb$ cap layer to prevent depletion of the QW by the surface states.

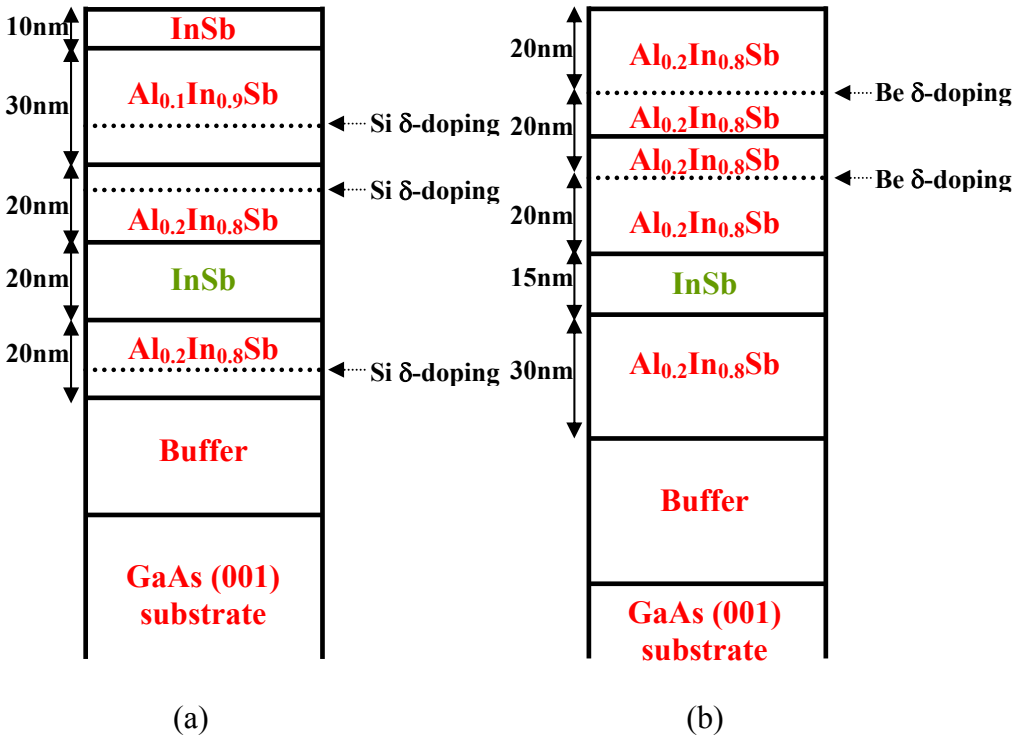

Figure 4.3 Cross sectional layout of the Al_xIn_ySb/InSb heterostructures (not to scale) (a): t340, Si δ-doped heterostructures. (b): t196, Be δ-doped heterostructures.

Doping of symmetric heterostructure (t340) was performed by introducing Si δ-doping layers on both sides of the well at a distance of 15 nm from the QW, resulting in zero electric field acting on the electrons along the growth direction (z direction). Samples, t196, t198, t200 and t250 are Be-doped wells. For all Be-doped wells, doping was introduced on one side of the well a distance of 20 nm above the QW. The hole then feels a non-zero electric field along the growth direction. This electric field then contributes to spin splitting at zero magnetic field. Other important details of the layers, and measured values for carrier densities and mobilities, are listed in Table 4.2. The carrier densities of the samples were obtained from standard Hall measurements performed in the HB geometry. The first and second subband energies of the above heterostructures were obtained from finite square well model solutions of the Schrödinger equation [65].

Table 4.2. Sample parameters: Well width, barrier width and Al concentration in barrier, buffer width and Al concentration in buffer, carrier density at 4.2K and mobility at 40K.

Samples labels	W_{QW} (nm)	Barrier width (nm), Al%	Buffer width (μm), Al%	Density (m^{-2})	Mobility (m^{-2}/Vs)	
					[100]	[110]
t340	20	15,20	1.8,20	4.0	4.8	4.2
t196	15	30,20	2,15	2.2	-	1.8
t249	12	20,20	3,15	4.0	-	3.6
t198	15	30, 20	2,15	4.9	-	1.8
t250	7	20,20	3,20	5.0	-	1.9

Both the non-parabolic effect of the conduction and the valence bands, and the effect of the strain were included to calculate the sub-band and Fermi energies. These values are summarized in Table 4.3 for each sample. For $InSb/Al_xIn_{1-x}Sb$ heterostructures, Dai *et al*. determined that the CB offsets were approximately 62% of the difference in the band gap energies [63, 64]. Consequently, barrier heights of InSb QW structure can be expressed as:

$$\Delta E_c = 0.62\left(2.06x_{barrier} - 0.157x_{barrier}\right)eV$$
$$\Delta E_v = 0.38\left(2.06x_{barrier} - 0.157x_{barrier}\right)eV \qquad 4.7$$

Where ΔE_c and ΔE_v are the conduction and valence barrier heights, respectively.

Table 4.3. Sample parameters: Subband energies were calculated using a non-parabolic expression. The sub band energies were obtained from finite square well model solutions. Ee,0 and Ee,1 are the first and second sub band energies for the electron. EHH,0 and ELH,0 are the first sub band energies for heavy and light holes

Samples	Subband energy (mev)		
	$E_{e,0}$	$E_{e,1}$	
t340	32	96	
		$E_{HH,0}$	$E_{LH,0}$
t196	10	5	38
t249	18	7	49
t198	23	5	38
t250	23	17	78

The experiments described in chapter 5 and 6 by means of low field transport measurements were performed using these five samples. The samples were measured at cryogenic temperatures using a four point bridge technique in a perpendicular magnetic field.

Chapter 5: Weak Anti-Localization in 2D and 1D n-Type InSb/AlInSb Systems

5.1 Introduction

Over the last two decades, it has been of interest to study both theoretically and experimentally the spin properties of 2DESs in addition to electronic properties [9-21, 43, 44, 53-69, 66-69]. The spin relaxation in 2DESs is governed by the D'yakonov-Perel (DP) mechanism through the Dresselhaus SOC [18]. In addition, asymmetric structures may also have a significant Rashba contribution [22, 28-30].

In 2000, it was suggested that the spin relaxation length of an electronic system can be significantly longer in quasi-1D channels than in 2D. This has been experimentally verified by several groups [20, 21, 56-60] in systems for which the anisotropic cubic term for Dresselhaus SOI was negligible relative to the isotropic linear term. Interestingly the cubic term is not suppressed by geometric confinement in quasi-1D systems, hence when both terms are relevant the remnant cubic coupling should lead to anisotropic spin relaxation in 1D channels. The experiment detailed in this chapter was focused on looking for this anisotropy via transport experiments using WAL analysis. The chapter is organized as follows. It begins with a discussion of experimental work on the SOI in the CB for InSb/$Al_{0.2}In_{0.8}Sb$ heterostructures. Next, experimental results on the suppression of spin relaxation as a function of reduced channel width is covered, followed by our observations on phase coherence in the InSb system.

5.2 Experiment

A symmetric InSb/$Al_{0.2}In_{0.8}Sb$ heterostructure (t340) was used for this series of experiments. The layer structure and characteristics of the heterostructure have been discussed previously in chapter 4. The sample was first processed into a Hall Bar (HB) mesa (see Figure 5.1(a)) in which HB channels were oriented along the two main crystallographic directions, [100] and [110], for a (100) growth plane. The width of the HB mesa and distance between the potential probes were 100 μm and 230 μm, respectively. After the optical lithography and etching of the mesa, arrays of quasi-1D wires were fabricated via EBL. Each wire array consisted of 30 identical wires of fixed wire width. The individual wires were 210μm long and were connected in parallel to reduce the effect of UCFs. Twelve sets of wire devices (of varying width) and two reference HBs were fabricated on the same chip within a $3.5mm^2$ area. Wire array widths (W_{EB}) varied from 700nm to 2000nm (as designed). Optical and SEM images of the wire arrays are shown in Figure 5.19(b). Standard Hall measurements at 4.2K gave the electron concentration which was the same ($n_e=4x10^{15}$ m^{-2}) along both the [100] and the [110] directions. The Fermi energy (E_F) calculated from n_e including non-parabolicity [Eq. 4.6] is 58 meV. The mobilities along the [100] and [110] directions at were 4.8 m^2/Vs and 4.2 m^2/Vs for [100] and [110] directions, respectively. This mobility anisotropy is consistent with the previous measurements of mobility anisotropy in our InSb/AlInSb heterostructures, which were attributed to preferential orientation of defects [70].

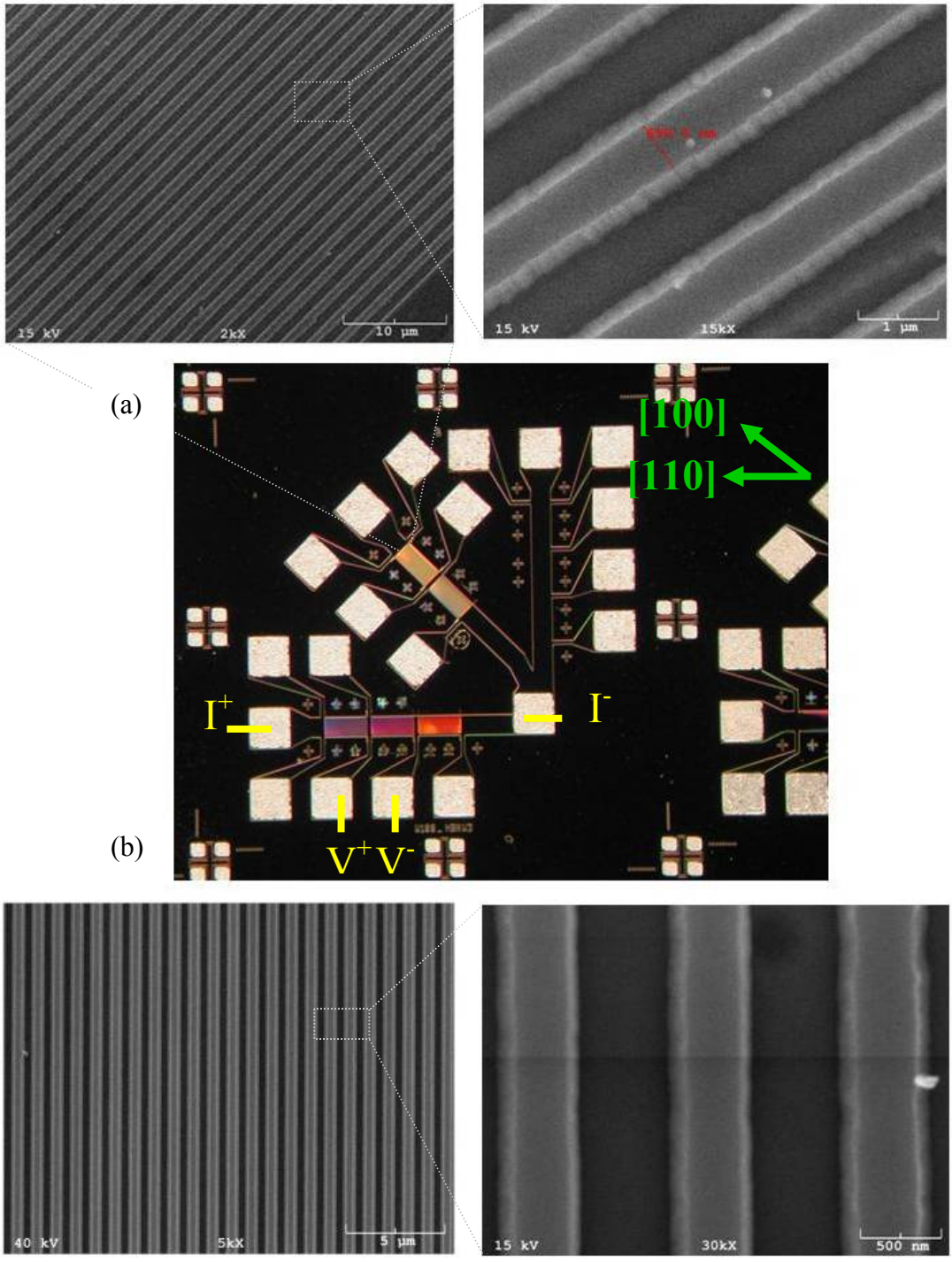

Figure 5.1 (a) Optical image of the device showing both unpatterned HBs and wire arrays. (b) SEM images of the narrow wires (SEM images are rotated by 90°).

5.3 Results and Discussion

5.3.1 2D Spin Relaxation Length

In order to carry WAL analysis of the unpatterned HB data to determine the 2D behavior of the spin relaxation length, the quantum correction first needs out to be separated from the measured low-field magneto-resistivity.

The resistivity, $\rho_{xx} = R_{xx} \times \frac{\text{Width of the Channel}}{\text{Length of the Channel}}$ was obtained and the non-oscillatory parabolic background contribution, $\left(1+(\mu_e B)^2\right)/\sigma_o$ (see Figure 5.2) was subtracted where $\sigma_o = n_e e \mu_e$ is the zero field conductance.

$$\Delta\rho_{xx}(B) = \frac{R_{xx} W}{L} - \frac{1+(\mu_e B)^2}{\sigma_o} \qquad 5.1$$

Using the relation, $\Delta\sigma_{xx}(B)=-\Delta\rho_{xx}(B)\sigma_o^2$, the resistivity was converted to conductance and the quantum correction was defined as:

$$\Delta\sigma = \Delta\sigma(B) - \Delta\sigma(B=0) = -\Delta\rho_{xx}(B)\sigma_o^2 \qquad 5.2$$

Figure 5.3 shows the low-field magneto-conductance correction for the 100 micron wide reference HBs in units of e^2/h after subtraction of the zero-field background, $\Delta\sigma(B)=\sigma(B)-\sigma(B=0)$: (a) shows the quantum correction for the two different orientations of the HBs at fixed temperature while (b) shows the quantum correction along the [100] direction at different temperatures. All conductivity traces show clear WAL peaks at zero magnetic field. The figure shows that the minima (B_{min}) in $\Delta\sigma(B)$, which is proportional to the strength of the

SOI, always at fixed field. For both directions, B_{min} was found at 1.2mT, thus, demonstrating the direction and temperature independence of the spin relaxation in 2D for this sample. The amplitude of the WAL peak is strongly temperature dependent, increasing with decreasing temperature from 10K to 1.5K. The amplitude of the correction will be used to determine the phase coherence length (L_ϕ) as a function of temperature at the conclusion of this chapter.

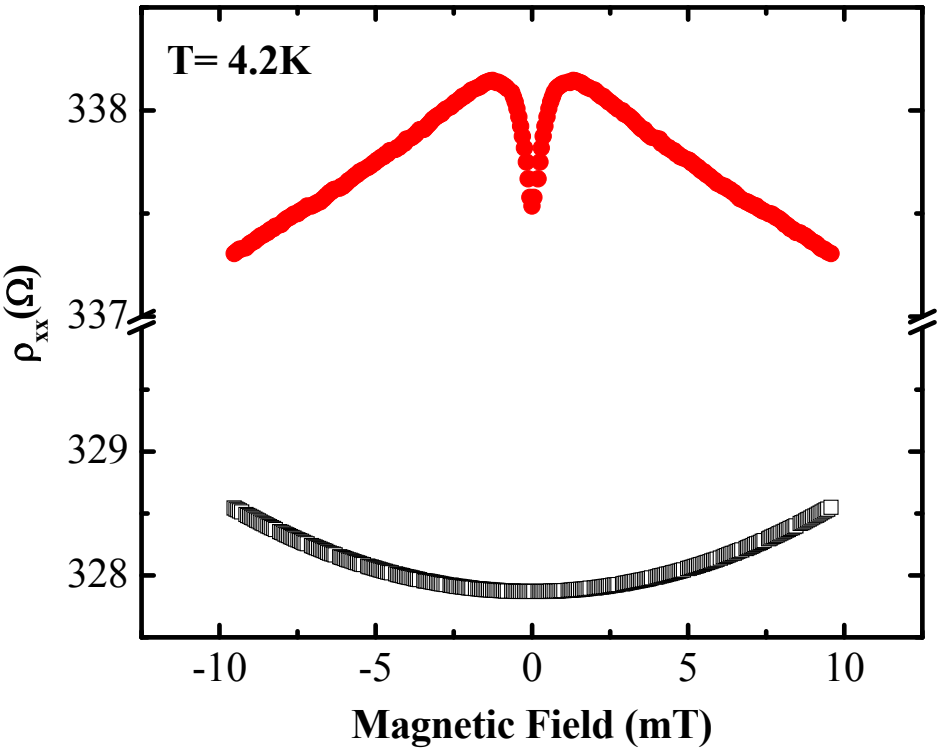

Figure 5.2 (a) Change of low field resistivity at T=3K. Open symbols are the measured magnetoresistance. Solid symbols are the parabolic background resistivity.

To evaluate the SO parameters for our 2DES, the electron momentum along the z direction was evaluated using the relation $k_z^2 = 2m(E)E_o/\hbar^2$ yielding $1.2x10^{16}m^{-1}$. Here, E_o is the first sub-band energy obtained from a finite square well model

with a non-parabolic mass. The average Fermi wave vector $k_F \left(= \sqrt{2\pi n_e}\right)$ was determined from the 2DEG carrier concentration n_e. These values lead to $\left(\left\langle k_z^2 \right\rangle - k_F^2/4\right) \Big/ k_F^2/4 \approx 0.83$ for sample t340; thus the cubic Dresselhaus is expected to provide a significant contribution to $\Delta\sigma(B)$, and cannot be excluded from WAL analysis. Therefore both linear and cubic terms in the ILP model (Eq. 2.34(b)) were included. Since the elastic mean-free path (L_e=0.47μm) of the 2DEG is small compared to the magnetic length (L_m=0.74 μm), transport in the sample is mostly diffusive (L_e<L_m) rather than ballistic and ILP model is appropriate The solid lines in Figure 5.3 are the best fits of equation 2.34(b) (ILP model) to the data $\Delta\sigma(B)$, with four adjustable parameters $\Delta\sigma(B=0)$, H_Φ , H_{so} and H'_{so}. The extracted values for H_{so} and H'_{so} are constant over the temperature range studied, while H_Φ increases with increasing temperature (as expected for the phase breaking length). The fitting results obtained at 4.2K are presented below in Table 5.1.

Table 5.1. The magnetic field parameters of the best fit for the experimental data presented in Figure 5.3 (a).

Directions	H_{so} (mT)	H'_{so} (mT)
[100]	0.56	0.544
[110]	0.64	0.572

Since our heterostructure is nominally symmetric, we assumed that the leading linear spin splitting term is due to the Dresselhaus spin interaction. Using the experimentally obtained values of $2|\Omega|^2\tau_1 = 4.34\text{x}10^{11}$ s^{-1} ([100]) and $2|\Omega|^2\tau_1 = 4.41\text{x}10^{11}s^{-1}$ ([110]); the Dresselhaus coefficient is the same for both crystallographic directions with a value of 520±20 eVÅ^3, in excellent agreement with the theoretical value (530 eV Å^3) estimated by Gilberston *et al*. for 20nm wide InSb QW with n_e=4 x10^{15} m^{-2} (i.e very similar to t340) [53].

Although the sample structure was designed to be symmetrically doped, a small Rashba contribution may be expected due to the preferential diffusion of the Si dopants along the growth direction. While for both linear contributions (Rashba and Dresselhaus), the spin splitting is isotropic in k-space, because of their different physical nature, they cannot be easily separated in models for the quantum conductivity correction.

Using the extracted values for H_{so} and H'_{so}, the zero-field spin splitting energies of the CB, $\Delta E_{so} = \sqrt{4\hbar^2 D/\tau_e L_{so}^2}$, were calculated. The elastic scattering time, τ_e $\left(=\mu_e m_e^*/e\right)$ was determined from the 2DEG carrier mobility μ_e and where D $\left(=\hbar^2 k_F^2 m_e^{*2}\tau_e/2\right)$ is the diffusion constant. Using the above Δ_{so} expression, calculated zero-field spin splitting energies are ≈1.6 meV and 1.7 meV for [100] and [110] directions, respectively. As a consequence, the strength of the Dresselhaus SOI relative to the Fermi energy, Δ_{so}/E_F, is 30% for t340 and is

comparable to the value of Δ_{so}=1.8meV (n_e~5.0x$10^{15}$$m^{-2}$) estimated for a $InSb/In_{0.85}Al_{0.15}Sb$ symmetric 2D electron system by Kallaher et al. [56].

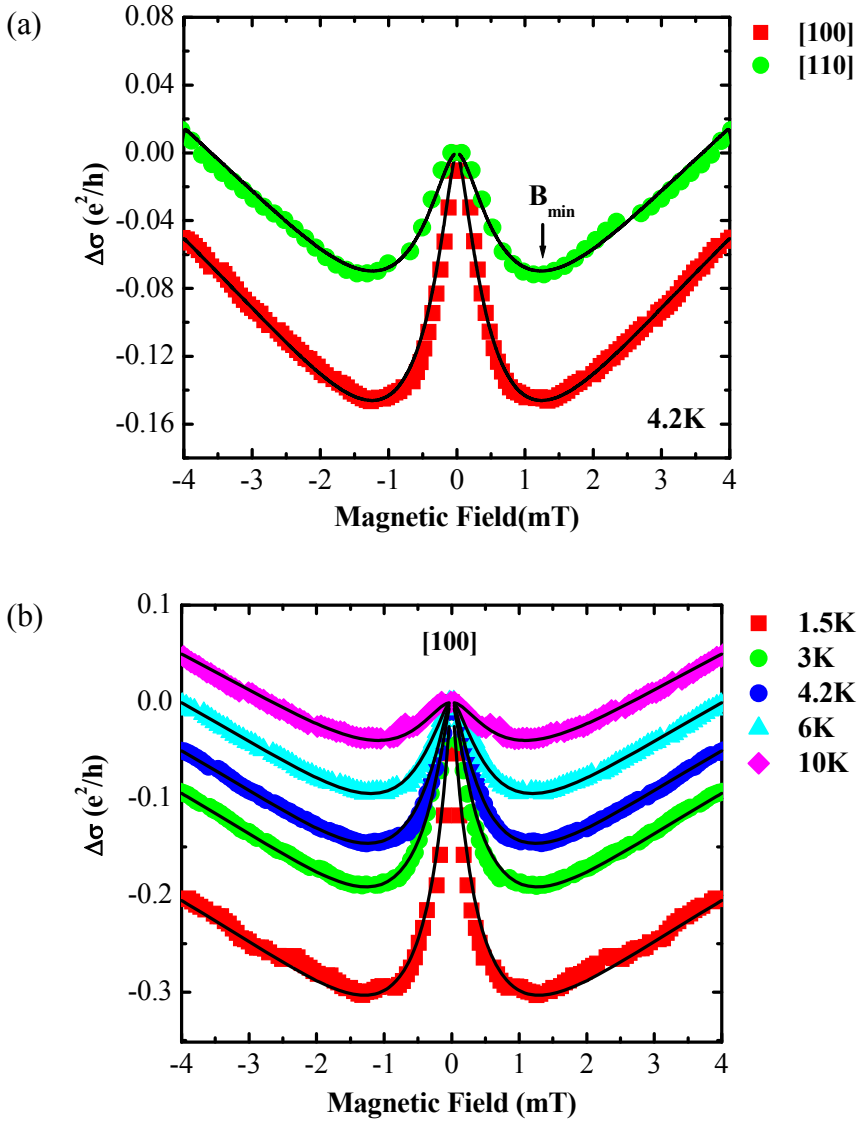

Figure 5.3 (a) Low-field magneto-conductance correction as a function of magnetic field: (a) at fixed temperature. The arrow indicates the WAL minima, (B_{min}) (b) at different temperatures. Solid symbols are the experiment data and black solid lines are the best fits to the ILP theory for WAL analysis when both linear and cubic terms are taken into account. The fitting SO field parameters, H_{so} and H'_{so}, at 4.2K are given in Table 5.1.

From the experimental value of $\hbar/4eD(\Omega_{3\theta}^2\tau_3)$, the ratio of τ_1/τ_3 was calculated. As mentioned in section 2.4.1, the ratio (τ_1/τ_3) depends on the dominant carrier scattering mechanism. $\tau_1(=\tau_e)$, is the momentum scattering time derived from measured transport parameters, mobility and density, while τ_3 reflects a different weighting of the angular scattering (see section 2.4.1). For isotropic scattering, ratio approaches unity (τ_1/τ_3) = 1, while in the limit of small angle scattering as is the case for scattering from remote ionized impurities the ratio is larger, (τ_1/τ_3) = 9. Mishima *et al.* has reported that the dominant scattering in our InSb heterostructures are threading dislocations and micro-twins [71] resulting from the 15% lattice mismatch with the GaAs substrates. These defects intersect the QWs and result in large angle scattering. Our experimentally determined ratio was found to be (τ_1/τ_3) $\approx$1 to 2, consistent with the conclusions of Mishima *et al.*

5.3.2 Transport Properties of 1D InSb Wire Structures

We now turn to the transport properties for quasi 1D wires fabricated from the 2D system whose characteristics were reported above. The designed widths, W_{EB}s of the wires within the arrays ranged from 2000 to 700 nm; however, the effective widths W_{eff}, are narrower due to the effects of lithography and etch processing. In order to obtain the W_{eff} of the each wire array, zero-field resistances, R(0), of each array were measured at T=40K, where quantum interference effects can be safely ignored. In Figure 5.4, the zero-field conductance (1/R) of the wire at T=40K are displayed as a function of the designed W_{EB} for both crystalline directions.

As shown in the figure, the conductivity is linear as a function of wire width for both crystalline directions, thus, resistance, R, of the wires follows the simple relation, R=Resistivity x Length / (Width x Number of wires). The constant linear behavior also suggests that the product of mobility and carrier density is not dependent on the wire width.

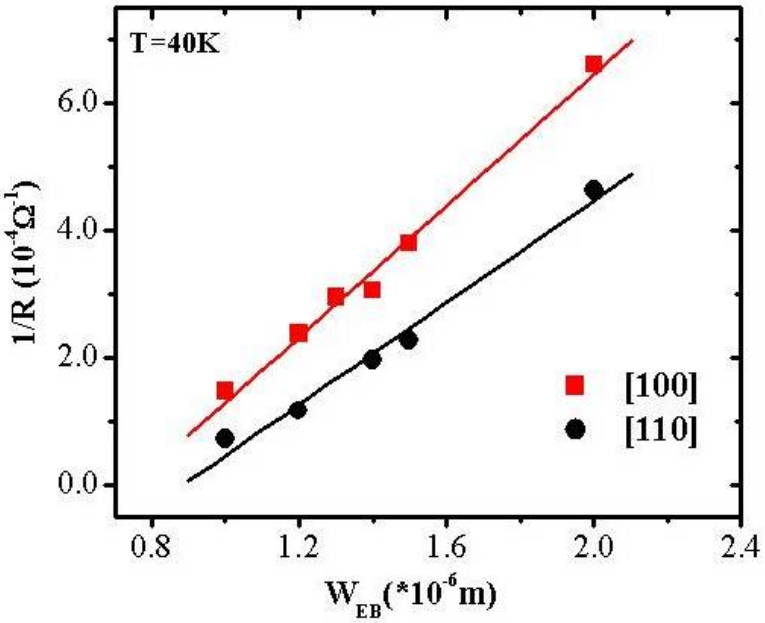

$$\frac{1}{R(40K)} = \frac{N}{\rho L} W_{EB} - \frac{N}{\rho L} W_{PE}$$

N – the number of identical wires

ρ – the resistivity of the 2DEG

L – the length of the wire

Figure 5.4 Zero field conductance at 40K as a function of design width (W_{EB}). Solid lines represent the corresponding linear fits.

As can be seen in the figure 5.4, the slopes are slightly different for both directions which we attribute to the different mobilities along the two directions as seen previously in the un-patterned HBs. Assuming that carrier concentration

was unchanged as a function of wire width and the same as the un-patterned HB, the mobilities calculated from slopes were 5.6 m^2/Vs and 4.4 m^2/Vs, yielding mean free paths of 0.58 and 0.46μm along the [100] and [110] directions, respectively.

The additional confinement resulting from processing effects and the depletion of carriers at the wire edges W_{pe}, was deduced from the x-intercept ; it can be seen that processing and depletion effects narrowed the wires a total of another 750 nm and 885nm along [100] and [110] directions, respectively. The effective depletion is half of this as each wire has two edges. By subtracting W_{pe} from W_{EB}, the effective wire width W_{eff}, for each array was determined.

5.3.3 1D Spin Relaxation Length

Figure 5.5 shows the low-field magneto-conductance corrections in units of e^2/h after subtraction of the zero-field background for 1D wire structures fabricated along the [100] and [110] directions at fixed temperature as a function of effective wire width. As can be seen, we always observed large signatures of the WAL effect. As the effective wire width is reduced, an anti-localization conductivity minimum (B_{min}) gradually moves to higher magnetic field. For the widest (1280 nm for [100] and 1115nm for [110]) wires, minima were always located at higher magnetic field than the minima for un-patterned HBs ($\pm B_{min}$=1.2 mT) (see Figure 5.6). Comparing the arrays along different directions, B_{min}s occurred at consistently lower field values for the [100] wires relative to the [110] wires. The

rate at which B_{min} changes with decreasing width, however, is the same for both directions and it has been found to vary as $W_{eff}^{-0.43}$.

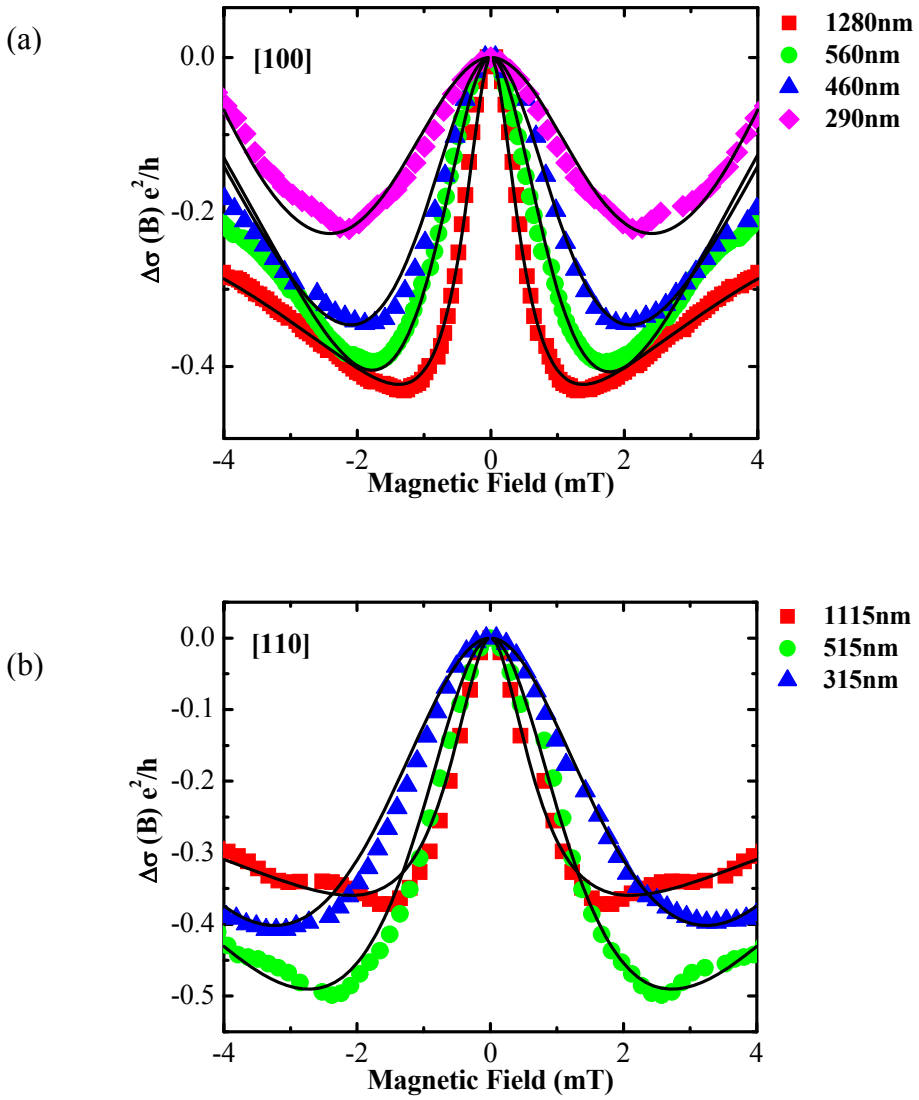

Figure 5.5 Low field magneto-conductivity correction vs. magnetic field for wire arrays orientated along the (a) [100] and (b) [110] directions at 4.2K. Solid symbols are the experiment data and the black solid lines are the best fits by equation 2.47 in section 2.4.4. The fitting length scales, $L_{so}(W)$ and $L_{\Phi}(W)$, are presented in Figure 5.7.

Since the mean free path of the wires was comparable to the effective width, it was assumed that the electron transport was principally diffusive; thus the spin relaxation length of our wire structures was explored by fitting the experimental data to the 1D diffusion model described in section 2.4.4. Data fitting was done by adjusting $L_{so}(W)$ (spin-orbit) and $L_{\phi}(W)$ (the spin-orbit and phase breaking lengths, respectively.) It can be seen in Figure 5.5 that our experimental data can be fitted very well by the 1D diffusion model even if the electronic transport of some wire structures was in a cross-over regime between diffusive and ballistic transport. The values of $L_{so}(W)$ extracted from the fitting are plotted in Figure 5.7 as a function of $1/W_{eff}$.

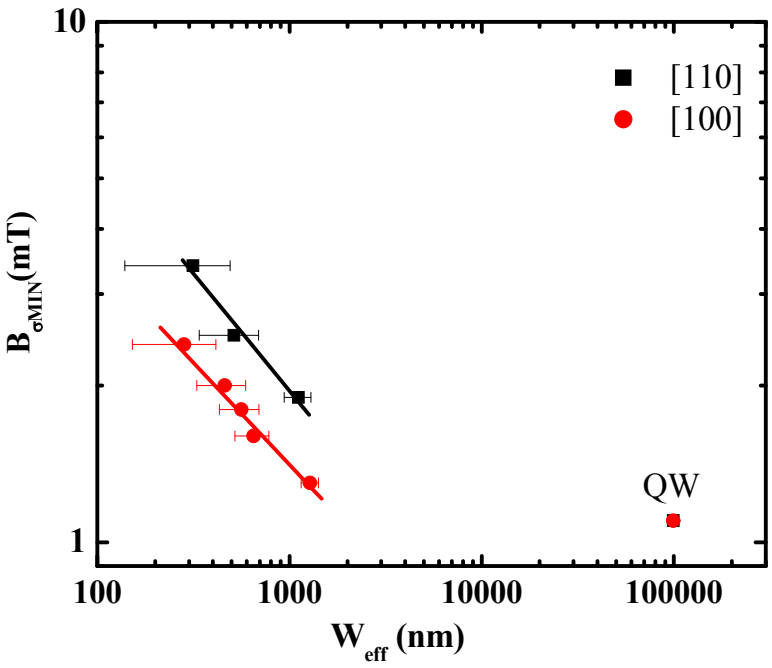

Figure 5.6 A log-log plot of the magnetic field location of the conductivity minimum as a function of effective wire width for arrays oriented along the [100] and [110] directions. Solid lines are provided as a guide for the eye.

As is seen in Figure 5.7, $L_{so}(W)$ is inversely proportional to channel width and was always found to be larger than the calculated bulk spin precession length L_{so}(~0.43 μm) for the 2DEG. The increase in $L_{so}(W)$ with decreasing channel width is attributed to dimensional confinement effects that have been previously predicted [53-55] and observed experimentally for narrow wires [20, 21, 56-60].

Additionally it is noted that the values of $L_{so}(W)$ extracted for the [110] direction are 30% shorter than those for the [100] direction, indicating an additional spin relaxation contribution for the [110] with an anisotropic cubic Dresselhaus term predicted to be maximal along [110].

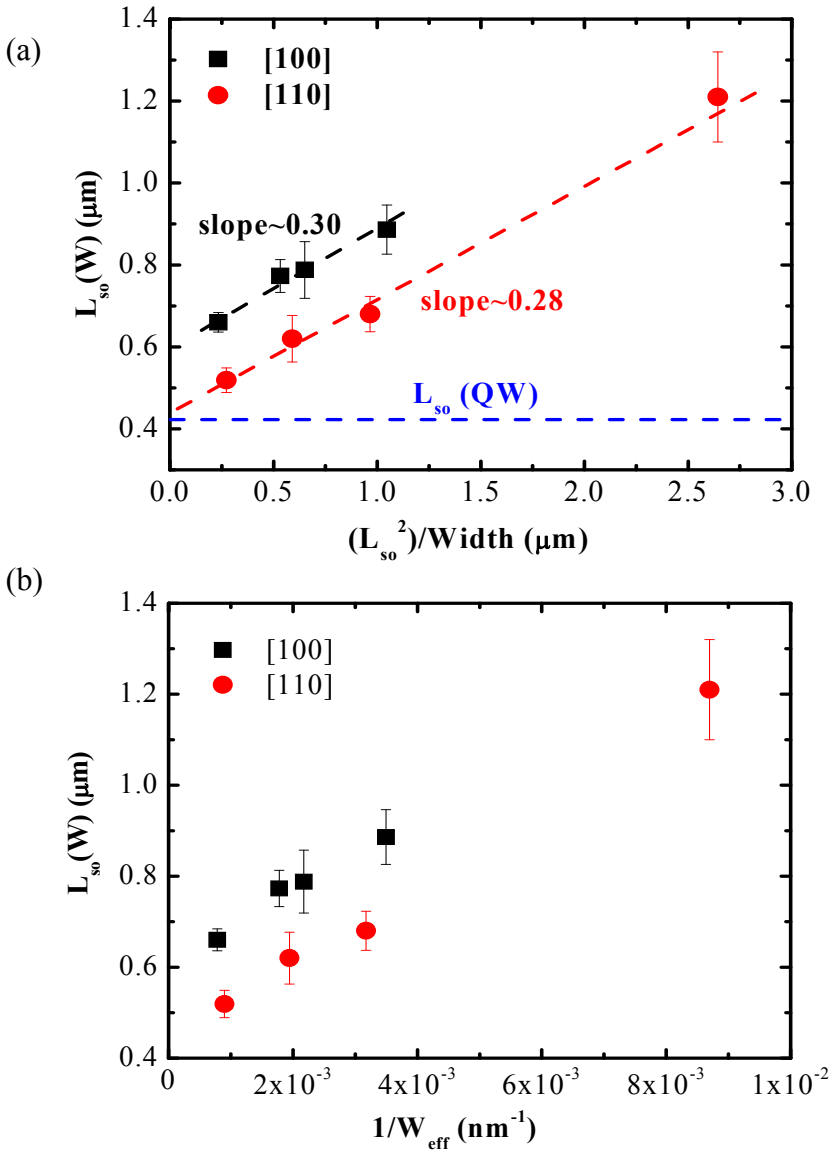

Figure 5.7 (a) Spin relaxation length of the wire as a function of the wire width along two crystalline directions. Solid symbols are extracted $L_{so}(W)$ from the fit of the experimental data by equation 2.47. (b) Spin relaxation length of the wire as a function of the (L_{so}^2/wire width) along two crystalline directions. The black and red dashed show linear fits. The blue dashed line is 2D spin precession length, L_{so} value obtained from the ILP fitting on the unpatterned HB.

Furthermore, our transport measurements are consistent with previous optical measurements of spin lifetime in symmetrically doped InGaAs wire structures, in

which the spin lifetime along the [110] direction was observed to be shorter than along the [100] direction [21]. Our data are repotted in Figure 5.7(b) as a function of (L_{so}^2/W_{eff}) together with the L_{so} value obtained from the ILP model for the unpatterned HB. $L_{so}(w)$ is linear in L_{so}^2/ W_{eff} with slope of 0.30 and 0.28 along the [100] and [110] directions, respectively. According to Ketteman's the expected, slope is 0.55 for any crystallographic direction (see equation 2.44). Thus, experimental results are in good agreement with theoretical predictions.

5.3.4 Electron-Electron Interaction

Our data can also provide information on phase coherence in 1D and 2D. Theories of 2DES have shown that the inelastic scattering events leading to phase breaking are dominated by electron-phonon and electron-electron scattering with the total phase breaking rate;

$$\frac{1}{\tau_{\Phi}} = \frac{1}{\tau_{e-p}} + \frac{1}{\tau_{e-e}} \quad \ldots 5.3$$

where, τ_{e-p} and τ_{e-e} are the electron-phonon and electron-electron scattering times, respectively. At low temperature, the electron-phonon interaction becomes negligible and the electron-electron interaction is the dominant inelastic scattering process.

5.3.4.1 Phase Breaking Length of the 2D Systems

The contribution of electron-electron scattering to the phase breaking has two limits depending on the degree of disorder and are described by the following expressions [72,73]:

$$\frac{1}{\tau_\Phi} = \frac{D}{L_\Phi^2} = \frac{\pi}{2}\frac{(k_B T)^2}{\hbar E_F}\ln(\frac{E_F}{kT}) \qquad \text{for} \quad T > \frac{\hbar}{k_B \tau_e} \tag{5.4}$$

$$\frac{1}{\tau_\Phi} = \frac{D}{L_\Phi^2} = \frac{k_B T}{2\pi\pi_o D\hbar^2}\ln(\pi D N_o \hbar) \quad \text{for} \quad T < \frac{\hbar}{k_B \tau_e} \tag{5.5}$$

where, $N_0 = m_e^* / \pi\hbar^2$ is the 2D density of states and D is the diffusion coefficient and the time τ_e is the momentum scattering time. When disorder is weak the momentum scattering time is long and $T > \hbar/k_B\tau_e$ over a large range of temperature leading to T^2 dependence for $1/L_\Phi{}^2$. When disorder is strong, the opposite limit is relevant $T < \hbar/k_B\tau_e$ and $1/L_\Phi{}^2$, is proportional to T.

For our sample, the factor, $\hbar/k_B\tau_e$, is ≈14K, larger than the highest experimental temperature (10K) accessed. To explore the temperature dependence of the observed phase breaking length (L_Φ), [where H_Φ ($= \hbar/4eL_\Phi^2$), resulting from our WAL fits] was plotted against temperature in Figure 5.8 and 5.9. It was observed that the phase breaking length grew as the temperature decreased with a $T^{-1/2}$ dependence specifically (see figure 5.8).

$$L_{\Phi}(T) = 3.6x10^{-6}(mK^{1/2})T^{-1/2} \qquad 5.7$$

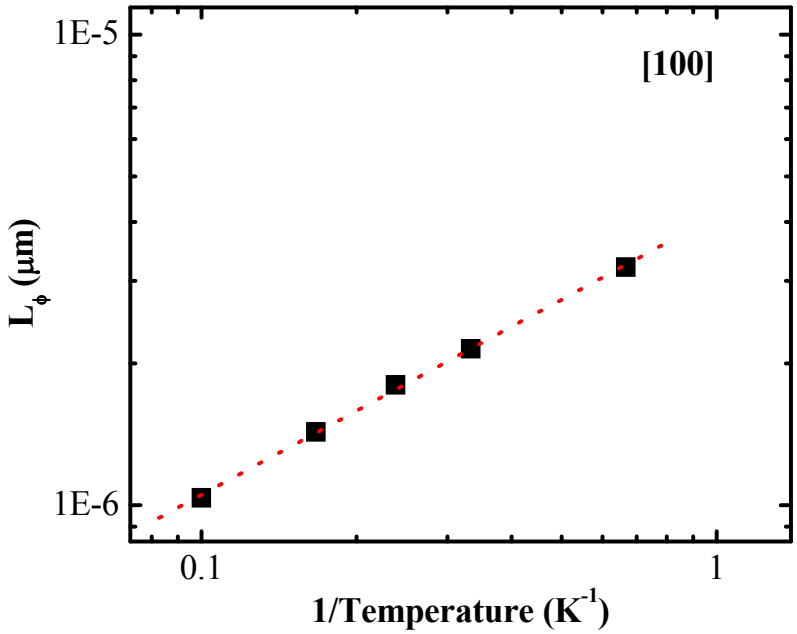

Figure 5.8 The phase breaking length (L_Φ) obtained from the fit of the experimental data by the ILP equation 2.34(b) in section 2.4.1 as a function of temperature.

For comparison, theoretically predicted $L_\Phi(T)$ using the pre-factor of the linear term of expression 5.5. yields

$$L_{\Phi}(T) = 6.0*10^{-6}(mK^{1/2})T^{-1/2} \qquad 5.8$$

and is shown as the dashed line in Fig. 5.9 The comparison shows that the experimentally determined $L_\Phi(T)$ is ≈ 1.6 times smaller than the predicted values. While our measured $L_\Phi(T)$ are smaller than predicted, our results are in

reasonably good agreement with theory for electron-electron scattering in the strong disorder limit.

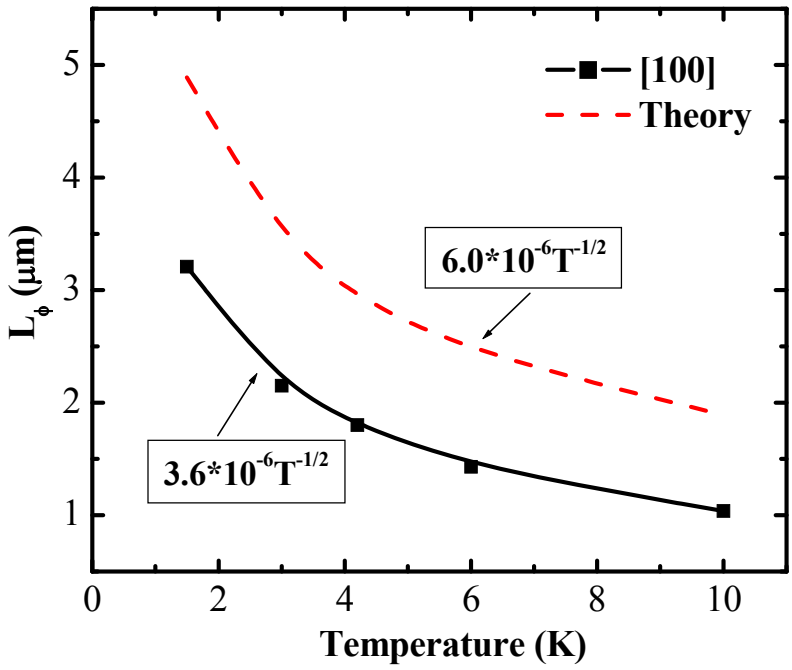

Figure 5.9 The phase breaking length (L_Φ) obtained from the fit of the experimental data by the ILP equation 2.34(b) in section 2.4.1 as a function of temperature. Dashed line is the theoretical fit to equation 5.5.

5.4.3.2 Phase Breaking Length in 1D Systems

We can do a similar study on our 1D wire arrays. In 1D channel, electron-electron scattering in the weak disorder limit is unchanged by dimensional reduction and equation 5.4 remains. The strong disorder limit however, experiences dimensional crossover as was first predicted by Thouless for wires at finite temperature and is given by [73]:

$$\frac{1}{\tau_\Phi} = \frac{D}{L_\Phi^2} = \left(\frac{k_B T}{D^{1/2} W N_o \hbar^2} \right)^{2/3} \quad \text{for} \quad T < \frac{\hbar}{k_B \tau_e} \quad \text{when } W < \pi L_T \tag{5.9}$$

where, $L_T = \sqrt{\hbar D / k_B T})$ is the thermal diffusion length. Temperature dependent $\Delta\sigma(B)$ were measured for all the arrays, are displayed in Figure 5.10 and 5.11 for both directions. Solid curves represent the fits using equation 2.47.

Extracted L_Φ from the fitting are summarized in Figure 5.12 as a function of temperature. When temperature is decreased, the L_Φ grows as seen previously in the 2D system [$\hbar / k_B \tau_e$ for [100] direction is ~11 and for [110] it is ~ 15] while our experiment was carried out over the temperature range from 10K to 1.5K. For our samples, πL_T valid between 1μm (1.5K) and 0.4μm (10K) and thus $W \sim \pi L_T$ implying that our data is in an intermediate regime between 1D and 2D, it is therefore not surprising that $L_\Phi \sim T^n$ $2/3<n<2$.

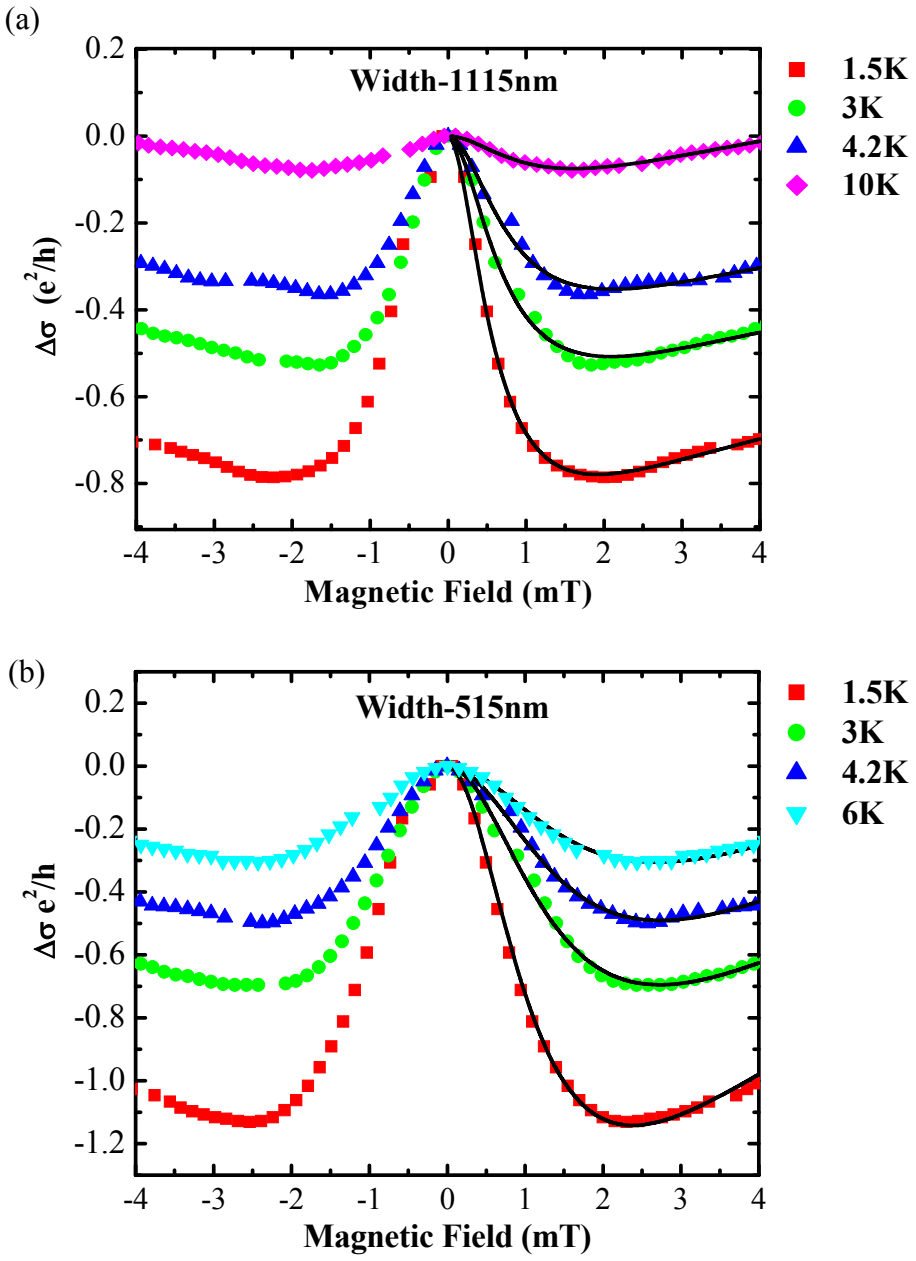

Figure 5.10 Temperature dependent magneto-conductance for 1D InSb channels for [110] direction: (a) 1115 nm wires, (b) 515 nm wires. The solid lines represent the fit by a 1D model from equation 2.47.

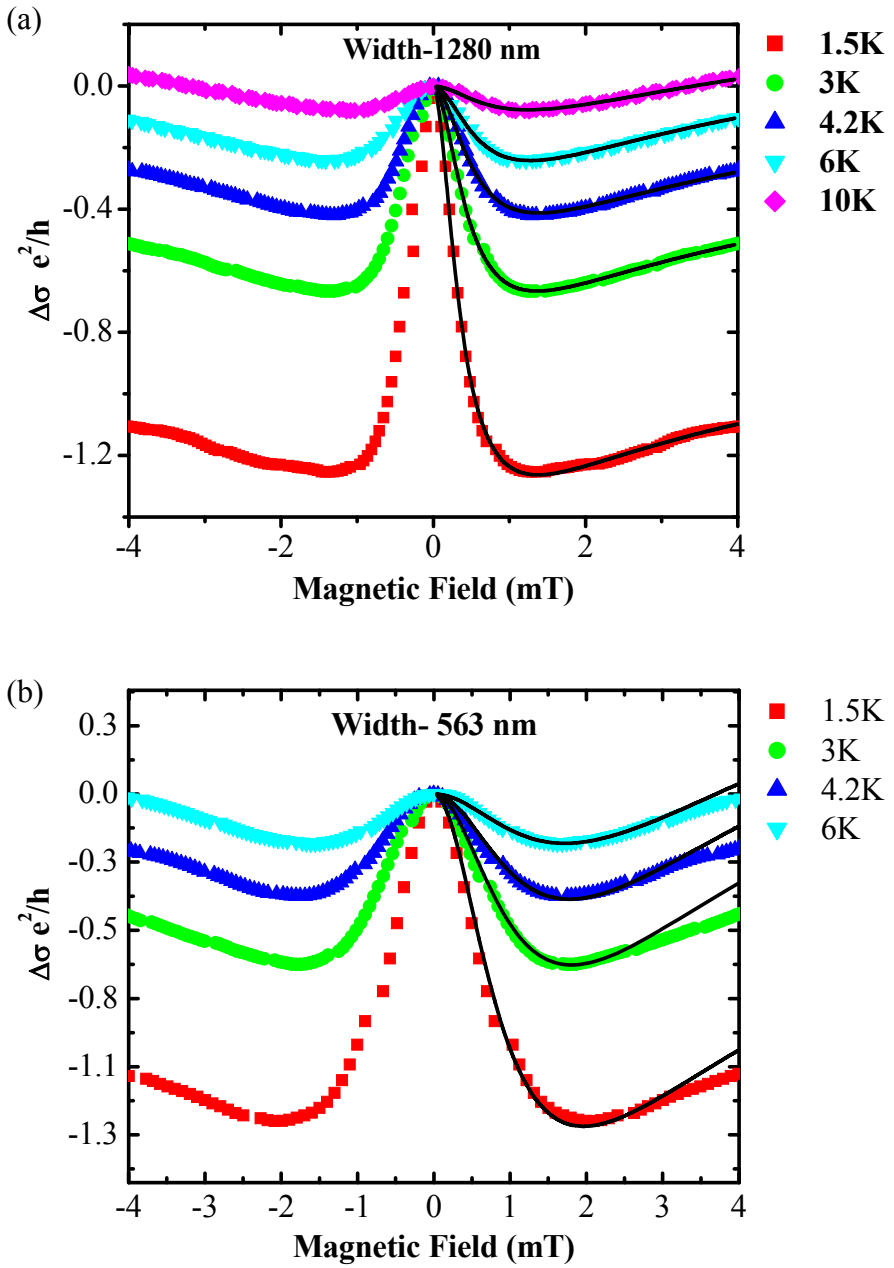

Figure 5.11 Temperature dependent e magneto-conductance for 1D InSb channels for [100] direction: (a) 1280 nm wires, (b) 560 nm wires. The solid lines represent the fit by a 1D model from equation 2.47.

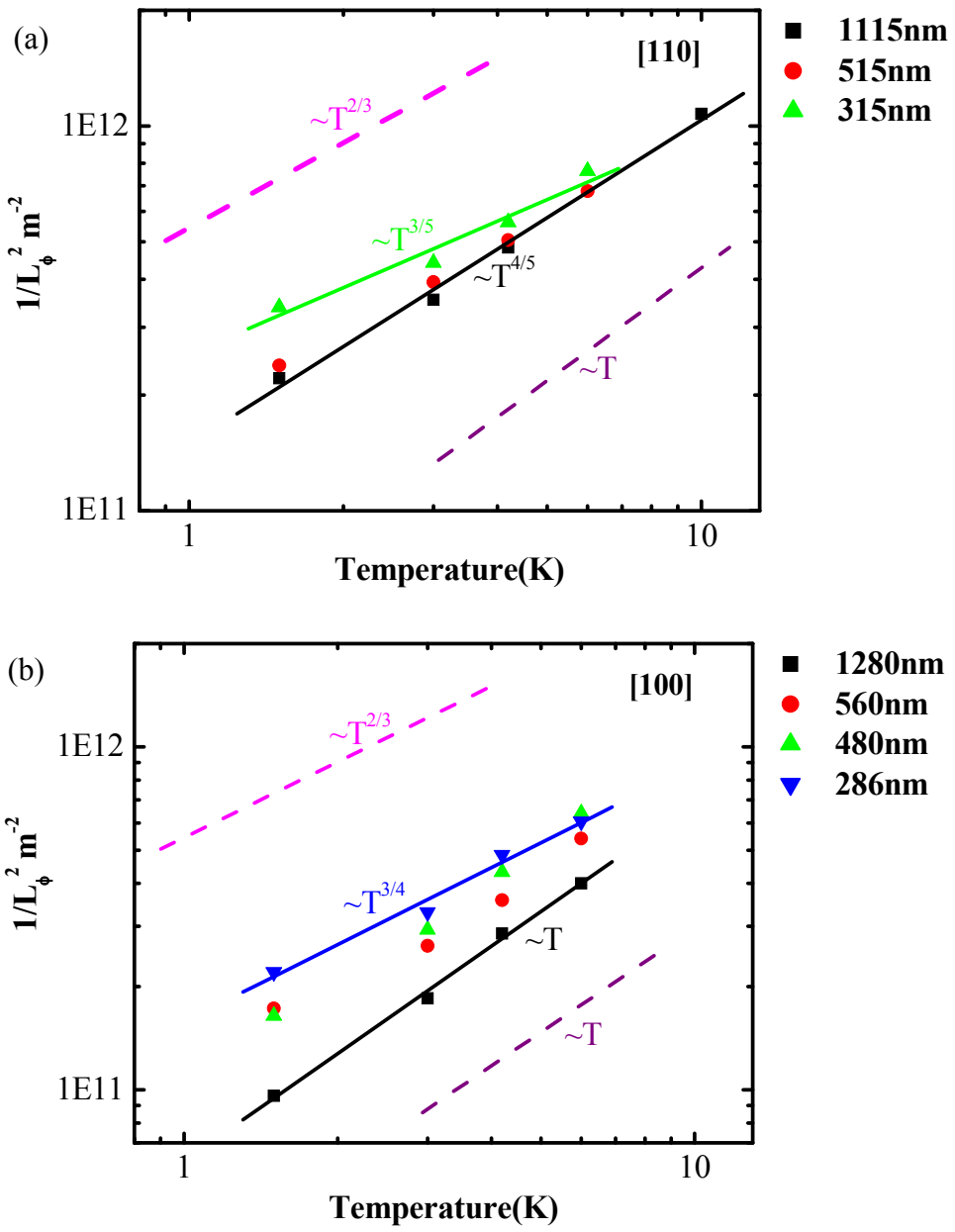

Figure 5.12 Temperature dependent phase breaking length extracted from the WAL analysis. Dashed lines are the theoretical slopes corresponding electron-electron scattering at low temperature, (strong disorder limit for 1D system $\sim T^{2/3}$ and strong disorder limit for 2D system ~T).

5.4 Conclusion

In conclusion, we have studied spin-orbit coupling in a single symmetrically doped InSb/$Al_{0.2}In_{0.8}Sb$ heterostructure using weak anti--localization (WAL) analysis in both the quasi-1D and 2D geometries. Both linear and cubic Dresselhaus contributions were included in the analysis of the 2D data. Our low temperature magneto-conductivity data yielded values of the Dresselhaus SO parameter and of τ_1/τ_3 in good agreement with theoretical predictions. Additionally over the temperature range studied a linear temperature dependence of the phase breaking rate indicated that the principal inelastic scattering mechanism was due to electron-electron interactions in the disordered limit. When quasi-1D confinement was imposed, suppression of spin relaxation was observed as the channel was narrowed. Channels aligned along the [100] direction displayed spin relaxation lengths ~30% longer than for wires aligned along [110] consistent with the additional influence of the cubic Dresselhaus. Additionally in the quasi-1D case, phase relaxation corresponds to a combination of both 1D and 2D behavior.

Chapter 6: Structural Induced Spin Splitting in 2D p-Type InSb/AlInSb System

6.1 Introduction

The study of the Rashba spin splitting in 2D systems has gained momentum over the last decade with the goal of controlling the spin precession in spin-based electronic devices. The Rashba spin splitting is proportional to the electric field that characterizes the inversion asymmetry for non-symmetric potentials [22, 28-30]. Until recently, this growing interest was focused almost exclusively on electronic systems, with rather limited theoretical and experimental work related to 2D hole systems [22, 42, 74-78]. Thus, the understanding of the Rashba spin orbit physics in 2D hole systems is still in the early stages.

The physics of the valence band is more complicated than that of the conduction band. The uppermost VBs have a total angular momentum J=3/2, with the HH and LH states defined by $j = \pm 3/2$ and $j = \pm 1/2$ respectively. Confinement in a QW lifts the VB degeneracy at k=0 and provides a preferential axis (the growth direction) for spin orientation. This competes with the in-plane orientation of the SO field and hence the physics is more involved, and confinement as well asymmetry influence the Rashba splitting. The two bands have different momentum dependence on the spin splitting, (k^3 for the HHs and k for the LHs) as described in theoretical work by Winkler *et al.*. Additionally the parameters can be tuned by geometry. The latter point has motivated our experiments to

investigate the spin properties of 2D hole systems by means of geometry, principally well width using WAL analysis.

6.2 Experiment

Four Be-doped $Al_{0.2}In_{0.8}Sb$/InSb heterostructures (t196, t198, t200 and t250) were investigated in this study. All four samples were asymmetrically doped and grown on GaAs substrates as described in section 4.2. The primary difference between the samples was the width of the QW and hole density. Sample parameters including well width, density and mobility were summarized in Table 4.2. All samples were processed into HB geometries (see Figure 3.3(b)) of width 50 μm or 100 μm with voltage probe separation of 230 μm between adjacent probes (L).

6.2.1 Results and Discussion

Figure 6.1 displays the magneto-conductance correction for our p-type AlInSb/InSb heterostructures at 3K. As seen previously in our 2DEG systems (Figure 5.3), clear WAL peaks can be seen. Anti-localization minima (B_{min}) for each sample are plotted in Figure 6.2. Compared to the 2DES, the observed B_{min} for the hole systems are very large, ranging from 4 to 16 mT, depending on the sample density and the width of the QW. There are two noteworthy features in this empirical data figure the first is the increase of B_{min} with increasing hole density; and the second is the increase of B_{min} with decreasing well width for comparable hole density.

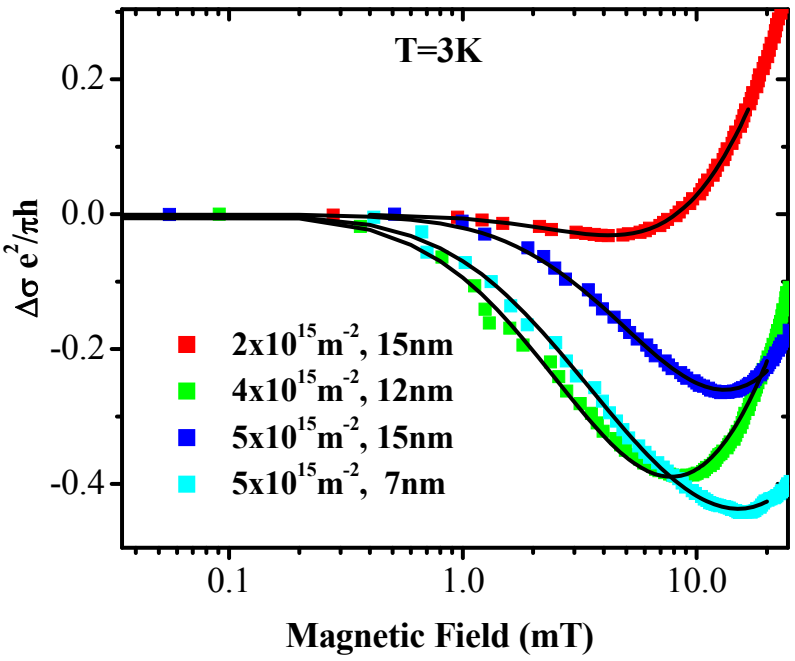

Figure 6.1 A semi-log plot of low-field magneto-conductance corrections as a function of a magnetic field at 3K. Solid symbols are the experiment data. Lines represent best fits using equation 2.34(b). The fitting field parameters, $H_{\|}$, $H_{\perp}$ and H_{Φ} are given in Table 6.1.

Before analyzing the data it is important to characterize the hole system. Our calculated values of E_0^{HH} and E_0^{LH} are summarized in Table 4.3. Fermi energies of these p-type systems are quite small relative to comparable electronic system due to the large effective hole mass. Our calculated values show that $E_0^{HH} << E_F << E_0^{LH}$, indicating that only the lowest sub band in the QW is occupied. In general, in structures studied here, both Rashba and Dresselhaus SO effects are expected, however, in the lowest sub band (HH), the Dresselhaus contribution is linear in the wave vector and thus is less significant at large hole

densities than the k^3 dependent Rashba term; hence, we presume that the Rashba contribution dominates.

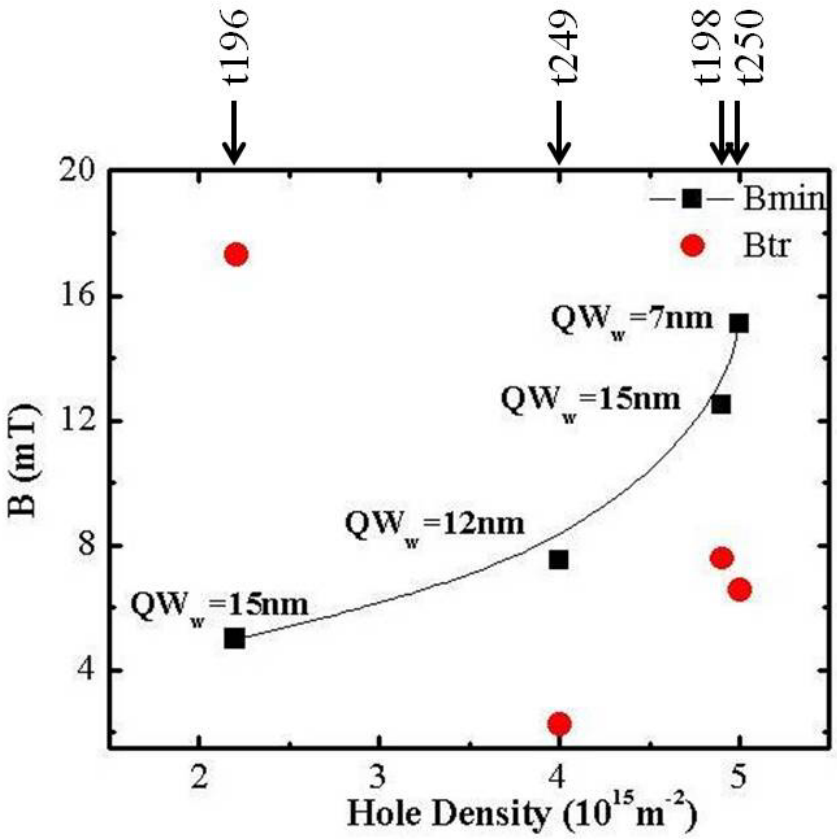

Figure 6.2 The positions of the minima in the magneto-conductivity (B_{min}) and transport fields (B_{tr}) as function of the hole density. A solid line is provided as a guide for the eye.

According to work by Winkler, the Rasbha coefficients for the VB can be written as shown in equations 1.16 a) and 1.16 b) of this thesis. Term 1.16 b) exceeds term 1.16 a) by a factor of ~30, hence we have only considered the former which contributes to the spin splitting as:

$$E\Delta_{so} = \gamma_{54}^{HH} E_z k_F^3 \qquad 6.1$$

where k_F is the average Fermi wave vector, which was determined from the measured 2D hole density: $k_F = \sqrt{2\pi n_p}$ and E_z is the electric filed which characterizes the inversion asymmetry of the sample,

$$E_z = \frac{1}{2}\frac{en_p}{\varepsilon\varepsilon_o} \qquad 6.2$$

where ε is the dielectric constant of the InSb (ε ~18), and ε_o is the vacuum permittivity.

To extract parameters related to the heavy hole Rashba spin splitting, the low field experimental data was analyzed using a model originally developed by Averkiev *et al*. (AGP) (see section 2.4.2). This model allows us to perform a fit to data by taking the spin relaxation fields, $H_{\shortparallel}$, $H_{\perp}$, and phase breaking field, H_{Φ}, as adjustable parameters. As mentioned in section 2.4.2 the AGP model is appropriate in the diffusive regime where the mean free path length is smaller than the magnetic length $L_e < L_m$. This sets a lower bound for the magnetic field range over which the theory is valid, $B < B_{tr}$ where $B_{tr} = \hbar/2eL_e^2$. Both B_{tr} and B_{min} are plotted in Figure 6.2. The values of B_{tr} for the samples t200, t198 and t250, were small compared to B_{min} thus, their transport is more ballistic. Clearly it is preferable to fit the data over a field range that includes the conductivity minimum, however there is as of yet no model describing the crossover between the diffusive and ballistic regimes for WAL in the valence band; hence, all the data for p-type QWs in this chapter were analyzed by using the AGP model.

This approach was also taken by Pederesen *et al*. in their analysis of p-type GaAs QW, justified by their observation that the AGP model qualitatively describes the correct magneto-conductance even for $L_e \geq L_m$ [75]. The solid lines in Figure 6.1 are the best fits using the AGP model as described in section 2.39(d) and it can be seen that good agreement can be found. The values of the spin relaxation fields determined by this model are presented in Table 6.1. It is observed that $H_\perp$ grows with increasing doping asymmetry (as indicated by the increasing hole density) and decreasing confinement. Sample t198 has the largest $H_\perp$ as expected due to the highest doping level whereas sample t250 has the smallest $H_\perp$ and highest $H_{||}$ of the four samples studied, as a result of the largest confinement along the growth axis. Extracted values of ΔE_{so} are presented in Figure 6.3 vs. hole density.

Table 6.1. Optimal fitting parameters for magneto-conductivity data at 3K using the AGP model. $H_{||}$ and $H\perp$ are the spin-relaxation fields directed along and perpendicular to the growth direction. $H\Phi$ is the phase breaking field.

Sample ID #	H_ϕ (mT)	$H_{||}$ (mT)	$H_\perp$ (mT)
T196	0.17	1.7	1.8
T249	0.36	2.3	2.3
T198	0.87	4.1	4.1
T250	0.41	9.5	1.1

Experimental determination of the Rashba spin splitting for these samples was calculated using

$$\Delta E_{s0} = 2h\Omega^{R}_{7H\,7H}(k) = \sqrt{\frac{4eH_{\perp}h^{3}k_{F}^{2}\tau_{3}}{\tau_{1}m^{*}_{xy,HH}}} \qquad 6.3$$

where Field $H_{\perp}$ is the spin relaxation field perpendicular to the QW axis; $m^{*}_{HH} = m_0/(\gamma_1+\gamma_2) = 0.019m_0$ and the time τ_3 is associated with probability of scattering by an angle 3θ in the 2D plane. τ_1 is the elastic scattering time from mobility measurements and using $t_1/t_3 = 1$, the experimental results and theoretical values are plotted in figure 6.3. Good qualitative agreement is observed between theory and experiment. Samples (t196 and t198) with comparable well width display that Δ_{so} values increase with increasing hole density; while Δ_{so} for the narrow well (t250) is dramatically reduced over that of a comparable density but less confined well (t198) due to the increased HH-LH separation in the former. However quantitative agreement was not found, the magnitude of the Δ_{so} values, calculated using leading Rashba coefficient γ_{54}^{hh} for all four samples, were significantly larger than those from the experiment. Both experimental and theoretical issues may contribute to this quantitative disagreement. On the theoretical side, the model for Δ_{so} includes only the electric field term of Rashba, neglecting any possible interface contributions. These interface contribution terms, however, are estimated to be small (< 0.1meV) and opposite in sign to that of the electric field term, and thus can probably be ruled out as the principal source of discrepancy.

On the experimental side, the fitting has been deliberately extended beyond the diffusive limit due to the lack of a valence band model for WAL in the crossover regime, however for sample t196 as can be seen in figure 6.2 the sample was comfortably in the diffusive regime and the disagreement was still significant. Another possibility may lie in our assumption that we could neglect the Dresselhaus contribution, however the Dresselhaus SO term is linear in k for HH and should become even less important at the large hole densities explored in this experiment.

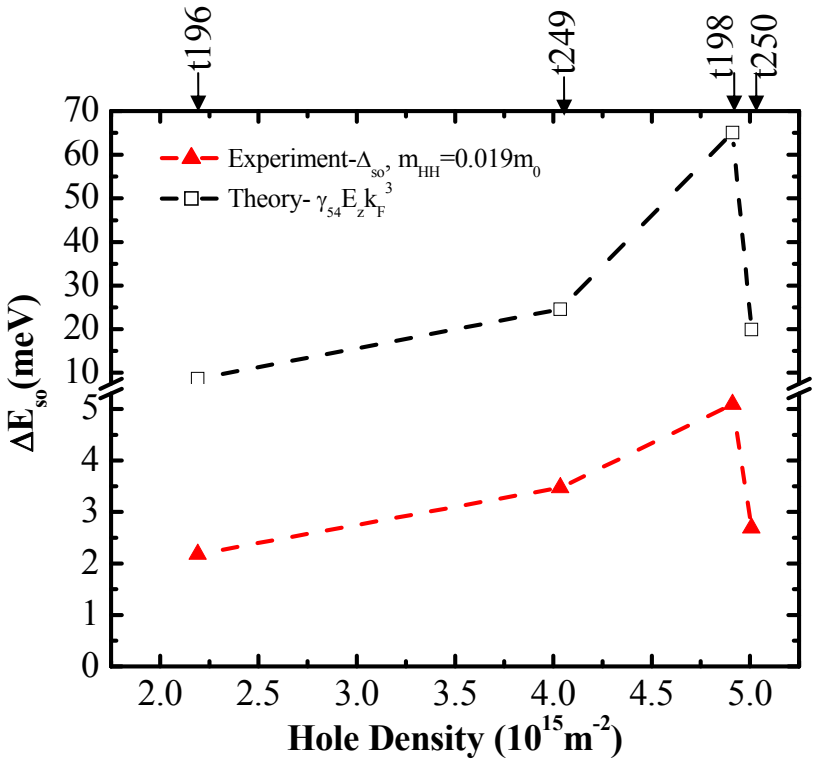

Figure 6.3 The ΔE_{so} values as function of the hole density for the four samples at a temperature of 3K. The theoretical values (open square: $\Delta E_{so}=\gamma_{54}^{HH} E_z k_{||}^3$ and solid triangles: experimental values) using the in-plane effective mass for the HH band, $m_{xy}^{HH} = m_0/(\gamma_1+\gamma_2) = 0.019 m_o$.

In addition, the experiment neglects the non-parabolicity of in-plane mass, rather a fixed in-plane mass was used for the determination of Δ_{so} from the WAL results; however, it is known that the in-plane HH mass increases with increasing strain, confinement and momentum for the valence band in a confined system due to an anti-crossing between the HH and LH. This however makes disagreement even larger. Thus only measuring the quantitative discrepancy, additional work is necessary both theoretically and experimentally to resolve the disagreement.

6.2.2 Conclusion

In conclusion, we have studied the Rashba spin orbit interaction in Be-doped InSb/AlInSb heterstructures by using a WAL analysis. Experimental curves were fitted to a model proposed by Averkiev for hole systems. Satisfactory qualitative agreement was achieved over a wide range of the QW geometry and densities of the 2D hole system. We observed that Δ_{so} values increase as the densities is increased and as confinement is reduced. The reason for the lack of quantitative agreement with theoretical expectations is not well understood; however, SO interface contributions, and in-plane hole mass dependence on strain, confinement and hole density may play a role. More theoretical and experimental work is required to fully understand this behavior.

Chapter 7: Conclusions and Suggestions or Future Work

7.1 Conclusions

In this dissertation, fabrication techniques and experimental studies performed in 2D InSb system are reported. Photo and electron beam lithographies, along with wet and dry etch techniques have been employed to fabricate the devices for electron and hole transport studies. Two separate transport experiments are described. Both experiments employ low temperature, low field magneto-transport measurements to explore the spin dynamics of low dimensional systems.

In the electron case, directional independent spin relaxation is observed for the [100] and [110] directions. The 2DES data was fit using a four-parameter ILP model, addressing both linear and cubic contributions. Resulting values of Dresselhaus constant 520±20 eVÅ^3 and the ratio of τ_3/τ_1 (1-2 range) are in good agreement with theoretical prediction (Gilbertson et al., 2008; Mishima et al., 2005). Additionally, using temperature dependent data for the [100] direction, the phase breaking length was found to vary inversely with temperature, as expected for electron-electron scattering in the strongly disordered limit.

To study the suppression of spin relaxation by geometrical confinement, quasi-1D wires were fabricated from the 2DES patterned along the [100] and [110] directions. Low field magneto-transport data were fit to a 1D model for the diffusive regime using the phase breaking (L_Φ(W)) and 1D spin relaxation lengths as fitting parameters (L_{so} (W)). An enhancement of the spin relaxation

length was observed as the channel was narrowed, and the spin relaxation lengths along the [100] direction were found to be approximately 30% longer than along the [110] direction. These observations are consistent with the dimensional confinement effect and the additional influence of the cubic Dresselhaus interaction along the [110] direction, respectively. Additionally, the dimensional dependence of the electron-electron scattering mechanism was investigated. Results showed that phase relaxation for narrower wires approaches the 1D limit, while that for wider wires is more 2D-like.

A second experiment investigated 2D holes. The Rashba spin orbit interaction in the valence band was studied by changing the hole density and QW width, i.e. changing the HH and LH band separation. The structures employed were asymmetric Be-doped QWs with varying hole density and confinement. The magnitude of the Rashba spin orbit coupling was determined using a model developed by Averkiev for p-type WAL analysis. Good qualitative agreement was observed as the ΔE_{so} values increased as the density was increased and as the confinement was reduced. The experiment, however, neglected effects of mass non-parabolicity and extended diffusive-WAL analysis into ballistic regime, while the model neglected the Dresselhaus component and interface terms. Perhaps due to these factors, the theoretical values for the spin-splitting overestimated the experimental values by ~five.

7.2 Suggestions for Future Work

Based on the experiments on geometrically confined electron systems reported in this dissertation, future work could continue the investigation of spin relaxation lengths and anisotropic spin relaxation. Narrower wires should display even longer spin relaxation lengths. It would be worthwhile to search for saturation of the spin relaxation length when relaxation is dominated by mechanisms other than the Dresselhaus terms, i.e. Elliot-Yafet mechanisms, etc. Additional work could also be performed on 2D hole systems. Spin-orbit effects are more complicated in the valence band separation and analysis is complicated due to the lack of sufficient theoretical work. Nevertheless, gated samples allowing a separate investigation of the HH and LH band separation and carrier density would be worthwhile.

References

[1] P.W. Anderson, Phys. Rev., 109, 1492, (1958).

[2] P. W. Anderson, E. Abrahams, and T. V. Ramakrishnan, Phys. Rev. Lett., 43, 718, (1979).

[3] G. Bergmann, Phys. Rev. Lett., 107, 1,(1984).

[4] S. Hikami et al., Prog. Theor. Phys., 63, 707, (1980).

[5] S. V. Iordanskii, Yu. B. Lyanda-Geller, and G. E. Pikus, JETP Lett., 60, 206, (1994).

[6] J. B. Miller, D. M. Zumbu¨hl, C. M. Marcus, Y. B. Lyanda-Geller, D. Goldhaber-Gordon, K. Campman, and A. C. Gossard, Phys. Rev. Lett., 90, 76807, (2003).

[7] L. E. Golub, Phys. Rev. B, 71, 235310, (2005).

[8] W. Knap, C. Skierbiszewski, A. Zduniak, E. Litwin-Staszewska, D. Bertho, F. Kobbi, J. L. Robert, G. E. Pikus, F. G. Pikus, S. V. Iordanskii, V. Mosser, K. Zekentes, and Y. B. Lyanda-Geller, Phys. Rev. B, 53, 3912, (1996).

[9] C. Schierholz, R. Kürsten, G. Meier, T. Matsuyama, and U. Merkt, Phys. Status Solidi B, 233, 436, (2002).

[10] T. Koga, J. Nitta, T. Akazaki, and H. Takayanagi, Phys. Rev. Lett., 89, 046801, (2002).

[11] Christopher Schierholz, Toru Matsuyama, Ulrich Merkt, and Guido Meier, Phys. Rev. B, 70, 233311 ,(2004).

[12] R. L. Kallaher and J. J. Heremans, Phys. Rev. B, 81, 075303, (2010).

[13] B. Grbic, C. Ellenberger, T. Ihn, K.Ensslin, D. Reuter, A. D. Wieck, Appl. Phys. Lett., 85, 2277, (2004).

[14] T. Hassenkam, S. Pedersen, K. Baklanov, A. Kristensen, C. B. Sorensen, and P. E. Lindelof, F. G. Pikus, G. E. Pikus, Phys. Rev. B, 55, 15, (1997).

[15] W. Desrat and D. K. Maude, Z. R. Wasilewski, R. Airey and G. Hill, Phys. Rev B., 74, 193317, (2006).

[16] Vitaliy A. Guzenko, Thomas Schäpers, and Hilde Hardtdegen, Phys. Rev B, 76, 165301, (2007).

[17] S.A. Studenikin, P.T. Coleridge, P. Poole, Physica E, 22, 349-352, (2004).

[18] C. Kurdak, N. Biyikli, Ü. Özgür, H. Morkoç, and V. I. Litvinov, Phy. Rev. B, 74, 113308, (2006).

[19] N. Thillosen, S. Cabañas, N. Kaluza, V. A. Guzenko, H. Hardtdegen, and Th. Schäpers, Phys. Rev. B, 73, 241311(R), (2006).

[20] Th. Sch¨apers, V. A. Guzenko, M. G.Pala, U. Z¨ulicke, M. Governale, J. Knobbe, H. Hardtdegen, Phys. Rev. B, 74, 081301(R), (2006).

[21] A. W. Holleitner, V. Sih, R. C. Myers, A. C. Gossard, D. D. Awschalom, Phys. Rev. Lett., 97, 036805, (2006).

[22] R. Winkler, Spin-Orbit Coupling Effects in Two-Dimensional Electron and Hole Systems (Springer-Verlag, Berlin, (2003).

[23] D. J. Reilly, Phys. Rev. B, 72, 033309, (2005).

[24] John David Jackson, Classical Electrodynamics, Third Edition.

[25] http://www.massey.ac.nz/~uzuelick/Cluster 09.pdf.

[26] G. Dresselhaus, Phys. Rev., 100, 2, 580, (1955).

[27] M. I. Dyakonov and V. I. Perel', Sov. Phys. JETP, 33, 1053, (1971).

[28] E. I. Rashba. Sov. Phys. Solid State, 2, 1109, (1960).

[29] Yu. A. Bychkov and E. I. Rashba. J. Phys. C: Solid State, Phys., 17, 6039, (1984).

[30] E. I. Rashba, Phys. Rev. B, 62, 267, (2000).

[31] G. M. Minkov, A. V. Germanenko, O. E. Rut, A. A. Sherstobitov,L. E. Golub, B. N. Zvonkov, and M. Willander, Phys. Rev. B, 70, 155323, (2004).

[32] F. G. Pikus and G. E. Pikus, Phys. Rev. B, 51, 16928, (1995).

[33] J. Kainz, U. Rössler, and R. Winkler, Phys. Rev. B, 70, 195322, (2004).

[34] N. S. Averkiev, L. E. Golub, and M. Willander, Semiconductors, 36, 91, (2002).

[35] A. M. Gilbertson, M. Fearn, J. H. Jefferson, B. N. Murdin, P. D.Buckle, and L. F. Cohen, Phys. Rev. B, 77, 165335, (2008).

[36] M. M. Glazov and L. E. Golub, Semiconductors, 40, 1209, (2006).

[37] J. Nitta, T. Akazaki, H. Takayanagi, and T. Enoki, Phys. Rev. Lett., 78, 1335, (1997).

[38] M. Cardona, N. E. Christensen, and G. Fasol, Phys. Rev. B, 38, 1806, (1988).

[39] S. Kettemann, Phys. Rev. Lett., 98, 176808, (2007).

[40] M. Studer, M. P. Walser, S. Baer, H. Rusterholz, S. Schon, S. Schuh, W. Wegscheider, K. Ensslin, and G. Salis, Phys. Rev. B, 82, 235320, (2010).

[41] C. Lü, J. L. Cheng, and M. W. Wu1, Physical Review B, 73, 125314, (2006).

[42] G. M. Minkov, A. A. Sherstobitov, A. V. Germanenko, O. E. Rut, V. A. Larionova and B. N. Zvonkov, Phys. Rev. B, 71, 165312, (2005).

[43] M. Cardona, N. E. Christensen, and G. Fasol, Phys. Rev. B, 38, 1806, (1988).

[44] G. Engels, J. Lange, Th. Schäpers, and H. Lüth, Phys. Rev. B, 55, R1958, (1997).

[45] N. W Ashcrot and N. D Mermin, Solid Stste Physics, (1976).

[46] H. van Houten, B. J. van Wees, M. G. J. Heijman and J. P. Andre, Appl. Phys. Lett., 49, 1781, (1986).

[47] C. W. J. Beenakker and H. van Houten, Solid State Physics, 44, 128, (1991).

[48] P. A. Lee and A. D. Stone, Phys. Rev. Lett., 55, 1622, (1985).

[49] G. Bergmann 1983 Phys. Rev. B, 28, 2917, (1983).

[50] G. Bergmann, Solid State Comm., 42, 815, (1982).

[51] W. H. Lau, J. T. Olesberg, and M. E. Flatté, Phys. Rev. B, 64, 161301(R), (2001).

[52] N. S. Averkiev, L. E.Golub, and G. E. Pikus, Solid State Commun., 107, 757, (1998).

[53] P. Wenk, S. Kattermann, Phys. Rev., 81, 125309, (2010).

[54] A. Kiselev and K. W. Kim, Phys. Rev., B 61, 13115, (2000).

[55] A. Bournel, P. Dollfus, P. Bruno, and P. Hesto, Eur. Phys. J.: Appl.Phys. 4, 1, (1998).

[56] R. L. Kallaher, J. J. Hermans, G. Goel, S. J. Chung, M. B. Santos, Phys. Rev. B, 81, 035335, (2010).

[57] P. Lehnen, Th. Sch¨apers, N. Kaluza, N. Thillosen, H. Hardtdegen, Phys. Rev. B, 76, 205307, (2007).

[58] A. Wirthmann, Y. S. Gui, D. Heitmann, C.-M. Hu, S. Kattermann, Physica E, 34, 493, (2006).

[59] V. A. guzenko, A. Bringerj. J. Knobbe, H. Hardtdegen and Th. Sch¨apers Appl. Phys. A, 87, 577, (2007).

[60] Th Schäpers, J Knobbe, V.A Guzenko, A van der Hart, Physics E, 21, 933, (2004).

[61] C. W. J. Beenakker and H. van Houten, Solid State Physics, 44, 128, (1991).

[62] C. W. J. Beenakker and H. van Houten Phys. Rev., B 38, No3, 3232, (1988).

[63] N. Dai, F. Brown, R. E. Doezema, S. J. Chung, K. J. Goldammer,and M. B. Santos, Appl. Phys. Lett., 73, 3132, (1998).

[64] N. Dai, G. A. Khodaparast, F. Brown, R. E. Doezema, S. J.Chung, and M. B. Santos, Appl. Phys. Lett., 76, 3905, (2000).

[65] J. H. Davies, The Physics of Low-Dimensional Semiconductors: An Introduction (Cambridge University Press, Cambridge, (1998).

[66] Junsaku Nitta, Tatsushi Akazaki, Hideaki Takayanag, Takatomo Enoki, Physica, E 2, 527, (1998).

[67] J.P. Heida, B.J. van Wees, J.J. Kuipers, T.M. Klapwijk, G. Borghs, Phys.Rev., B 57, 11911, (1998).

[68] Ç Kurdak, N. Biyikli, Ü Özgür, H. Morkoç, and V. I. Litvinov, J. Appl. Phys., 106, 103702, (2009).

[69] M. Schultz, F. Heinrichsy, U. Merkt, T. Colin, T. Skauli, S. Løvold, Semicond. Sci. Technol., 11, 1168, (1996).

[70] M. A. Ball, J. C. Keay, S. J. Chung, M. B. Santos and M.B. Johnson, Appl. Phys. Lett., 80, 2138, (2002).

[71] T.Mishima, J. Keay, N. Goel, M. Ball, S. Chung, M. Johnson, and M. B Santos, Journal of Vaccum Science & Techonology B: Microelectronic and Nanometer Structures, 23, 1171, (2005).

[72] H. Fukuyama and E. Abrahams, Phys. Rev. B, 27, 5976, (1983).

[73] K. Choi, D. C. Tsui, and K. Alavi, Phys. Rev. B, 36, 7751, (1987).

[74] N. S. Averkiev, L. E.Golub, and G. E. Pikus, Solid State Commun., 107, 757, (1998).

[75] S. Pedersen, C. B. Sörensen, A. Kristensen, P. E. Lindelof, L. E. Golub, and N. S. Averkiev, Phys. Rev. B, 60, 4880, (1999).

[76] N. S. Averkiev, L. E. Golub, and G. E. Pikus, Fiz. Tekh. Poluprovodn , semiconductors, 32, 1087, (1998).

[77] http://arxiv.org/ftp/arxiv/papers/1010/1010.3464.pdf.

[78] S. Faniel,1, B. Hackens,1 A. Vlad,1 L. Moldovan,1 C. Gustin,1 B. Habib,2 S. Melinte,1 M. Shayegan,2 and V. Bayot1, Phys. Rev. B, 75, 193310, (2007).

Appendix A: Photo Lithography Recipe

1. Cleave the sample into an 8x8mm^2 piece from the wafer.
2. Rinse the sample surface with acetone, methanol, and iospropanol, (IPA).
3. After cleaning the surfaces of the sample, blow dry with nitrogen gas.
4. Dehydration-bake at 150^{o}C for 15 minutes in a conventional oven.
5. Place the sample on the Al block and allow the sample to come to room temperature.
6. Spin coat AZ5124E photoresist at 4000 RPM for 40 seconds.
7. Soft-bake the sample at 95^{o}C for 60 seconds on a hot plate.
8. Expose sample under photo mask for 6 seconds with a 350W UV source *

(a) Positive step

i Develop in MIF 319 developer for 60 seconds.
ii Rinse the sample with DI water for between 1-2 minutes.
iii Hard-bake at 120^{o}C for 60 seconds on a hot plate.
iv Etch the sample before contact pads fabrication.
v Remove the resist with 1165 remover.
vi Rinse in flowing DI water.

(b) Negative step

i Post-bake the sample at 120^{o}C for 120 seconds on a hot plate*.
Ii Flood expose for 60 seconds with a 350W UV source.
iii Develop in MIF 319 developer for 60 seconds.
iv Hard-bake at 120^{o}C for 60 seconds on a hot plate.
v Evaporate contact material
vi Remove the resist with 1165 remover.
vii Rinse in flowing DI water.

Now * Time are 6.5 and 2.5 seconds in new recipe

Appendix B: Electron Beam Lithography Recipe

1. Rinse the sample surface with acetone, methanol, and isopropanol, (IPA).
2. After cleaning the surfaces of the sample, blow dry with nitrogen gas.
3. Dehydration-bake at 150^{o}C for 15 minutes in a conventional oven.
4. Place the sample on the Al block and allow the sample to come to room temperature.
5. Spin coat ZEP520 Electron beam resist at 5000 RPM for 45 seconds.
6. Pre-bake the sample at 170^{o}C for two minutes on a hot plate.
7. Expose sample using an area dose with 40keV electron beam
8. Develop in Xylenes for 45 seconds
9. Rinse the sample with IPA for 30 seconds.
10. Bake at 130^{o}C for 60 seconds on a hot plate.
11. Etch the sample.
12. Remove the resist with 1165 remover.
13. Rinse in flowing DI water.